Fatigue Performance Modeling in Advanced Out-of-Autoclave Composites for Aerospace Applications

A Thesis

By

GRAYSON REID CURRY

Presented to the Faculty of the Graduate School of

The University of Texas at Arlington in Partial Fulfillment

of the Requirements for the Degree of

MASTER OF SCIENCE IN AEROSPACE ENGINEERING

Chair of Committee: Dr. Endel V. Iarve

Committee Members: Dr. Ashfaq Adnan

                                      Dr. Andrew V Makeev

                                      Dr. Md Rassel Raihan

THE UNIVERSITY OF TEXAS AT ARLINGTON

May 2023

Abstract

Increased application of composite materials in the military and civil applications renewed the interest to development of high-fidelity methodologies for predicting their performance characteristics. Besides the traditional autoclave processed structural composites such as IM7/8552 and IM7/977-3 widely used on various platforms, novel materials such IM7/5320-1 suitable for Out-of-Autoclave (OoA) cure became of interest. Static and fatigue performance prediction of Open-Hole quasi-isotropic laminates made from IM7/5320-1 was performed in this work by using the Finite Element Analysis software BSAM. Progressive failure simulation including delaminations, matrix cracks and fiber failure was performed. Regularized eXtended Finite Element Methods (RXFEM) was used for mesh independent on-the-fly insertion of intralaminar matrix cracks. The Cohesive Zone Model (CZM), and the strength tracking methods were used for both inter and intralaminar crack propagation during fatigue loading. In addition, to capture the accurate stress ratio in each material point of the structure an algorithm for recoding local R-ratio was implemented. A Continuum Damage Mechanics (CDM) model was used for fiber failure initiation and propagation. It is the only damage mode modeled by CDM. Previously developed and validated static failure method was extended to fatigue damage prediction by applying S-N based strength reduction and proportional empirical reduction of the effective fiber fracture toughness in compression. The RXFEM methodology, previously applied to tension-tension cases was expanded to perform analysis under compression-compression and compression-tension loading conditions. Three different loading amplitudes were determined based on static strength. Delamination, matrix cracks, and fiber failure damage accumulation found during the fatigue analysis was compared with the experimental results found in the Advanced Material Characterization and Structural Certification (AMCS) Volume 1 by the

National Institute for Aviation Research (NIAR). All material properties required for analysis were provided by NIAR including static and fatigue properties. The results obtained under tension-tension loading showed the best correlation of extent and location of matrix cracks and delamination with the experimental data. Fiber damage was most notably found in the compression-compression model, predicting appropriate length in zero- and forty-five-degree plies. All three damage modes were observed in compression-tension in outer and zero-degree plies. The similarities and differences in computed results and experiment are discussed.

Acknowledgements

Table of Contents

List of Figures

List of Tables

1 Introduction

Composite materials have been at the forefront of the aerospace structures and the desire for stronger structures without a drastic increase in weight can be satisfied with advancements in laminate composites. However, the manufacturing and testing of laminate composites can be costly compared to the metallic counterparts. As new composites are developed, strength and fatigue tests must be performed to understand how the material will perform under expected loads and when the material might fail. The strength and fatigue tests executed account for a large portion of the cost and labor time, and any advancement in reducing both time and money is vital in expanding the functionality of composites.

Gaining a fundamental understanding and accurate prediction of failure and damage propagation under fatigue loading in laminate composites is pertinent before the material is introduced into application. Over the past few decades, advancements in numerical computation in the form of Finite Element Analysis, FEA, has allowed for material and structure testing with a reduction in physical experiments. Although computational advancements have eased the need for physical testing, further progress in the field can provide results with more accuracy and efficiency. Through the present work, damage evolution found through fatigue loading of IM7/5320-1 Open-Hole specimens will be analyzed using FEA software and compared with the experimental results found by the National Institute of Aviation Research. Three Open Hole cases will be studied Compression-Compression, Compression-Tension, and Tension-Tension with the emphasis on observing delamination, matrix cracks, and fiber failure.

1.1 Use of Composites in the Aerospace Industry

Composite materials were first introduced fifty years ago but were applied in a limited fashion, only being applied in sub-structures such as control surfaces [1]. As understanding of composites increased and the clear strength to weight ratio advantage to the common metals used, composites transitioned to being used in the primary structure of aerospace vehicles, namely wings and fuselages. A considerable jump was made in the transport industry with Boeing's release of the 787 comprising of more than fifty percent composite material, compared to eleven percent usage in the 787's running mate, the 777 [2]. A graphic depiction of the percentage of total weight comprised of composites in transport aircraft can be found in Figure **1.1**. Although composite materials are relevant in aerospace structures, an increased use can be found in other industries such as the automotive and sporting equipment industries.
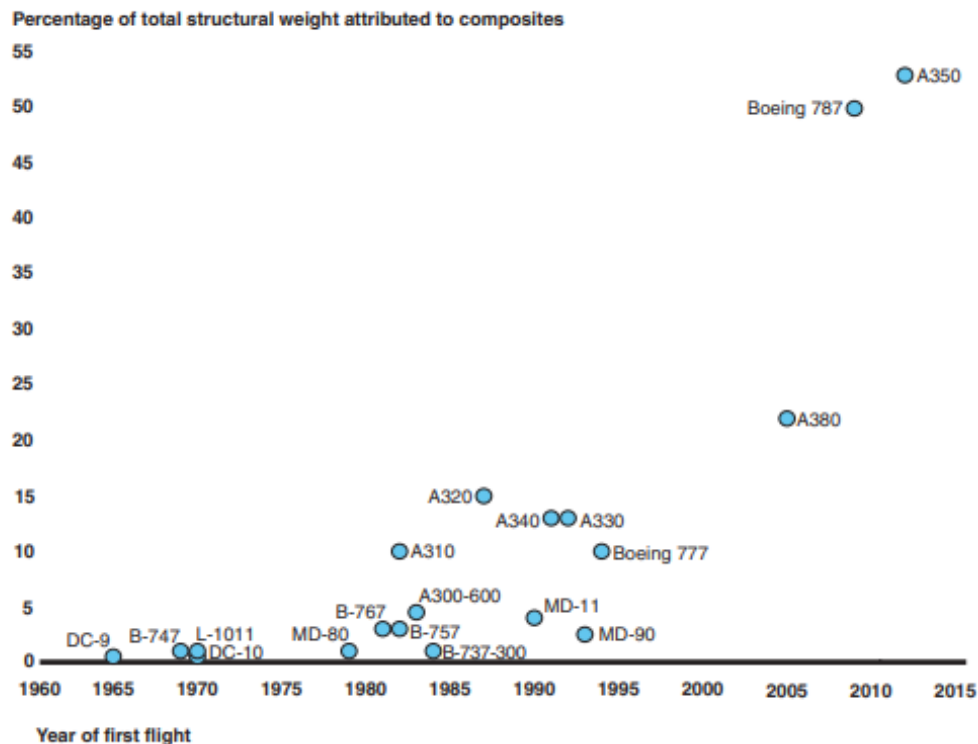
Figure 1.1 Composite Usage in Commercial Transports [3]

2

1.2 Mechanisms of Damage in Laminate Composites

Damage in laminate composites can be observed to be both interlaminar and intralaminar [4][5]. The amount of damage observed during testing can be affected by many factors, including the stacking sequence of the laminate and the endured loading. The present work will focus primarily on two intralaminar damage mechanisms, matrix cracking and fiber failure, and one interlaminar damage mechanism, interlaminar cracking, also known as delamination. Damage mechanisms often interact with each other and can be affected by loading factors such as cyclic and thermal loading. Fatigue and thermal loading can lead to more damage compared to traditional static loading, reducing the overall strength of the laminate composite over time. Furthering the understanding of mechanisms in damage of laminate composites is essential in improving the functionality of composites in the future.

1.2.1 Matrix Cracking

Matrix cracking is often the first form of damage observed in laminate composite testing and are often categorized as transverse, through the thickness, or in-plane cracking. Transverse cracking is commonly found in the off-axis plies, plies not aligned in the loading direction, because of weaker material properties than plies orientated in the loading direction [4,6,7]. Transverse cracking can lead to other damage mechanisms such as delamination in the interfacing plies.
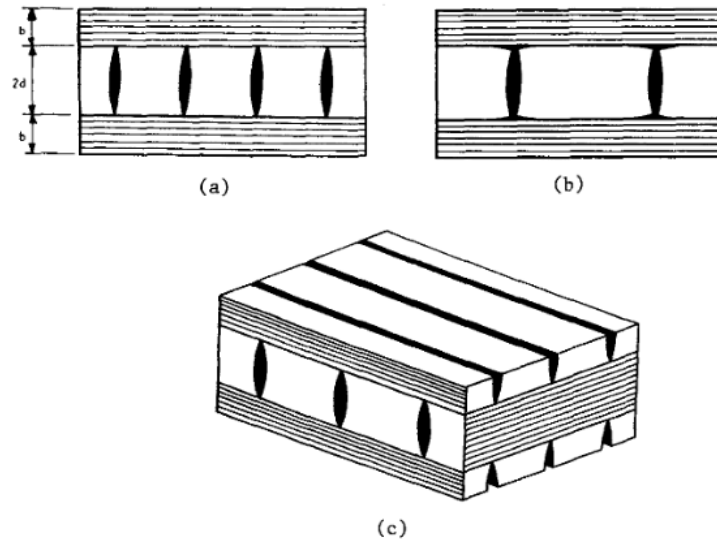
Figure 1.2 Matrix Cracking in Composite Laminates (a) Transverse Cracking, (b) Transverse Cracking and Delamination, and (c) In-Plane Cracking [6]

In-plane cracking can occur because of manufacturing defects in the matrix or debonding between matrix and fibers. In-plane cracks propagate in the direction of the fiber orientation of the ply and is affected by the stacking sequence of the laminate and is normally first observed in the off-axis plies, much like transverse cracking.

1.2.2 Delamination

Interlaminar cracking, or delamination, is cracking found between adhering laminas leading to separation between the plies. Delamination is often first observed at the free edges of laminates, including holes, and will be emphasized in the current work, where the interlaminar stresses are the highest [4,8]. Interlaminar cracking is primarily produced by the mismatch of properties of neighboring plies as fiber orientation is a major factor in the ply's strength, however, other factors i.e. manufacturing defects and even impact can lead to delamination [9]. As ply separation increases, the load carrying capacity of the laminate drastically decreases, leading to complete failure of the specimen. Matrix cracking and delamination are commonly

observed together in composite testing as the stress redistribution caused by matrix cracking leads to delamination and further delamination leads to the connecting of other matrix cracks. This cycle in turn leads to catastrophic failure of the laminate.

1.2.3   Fiber Failure

Fibers are the main load carrying material in laminate composites and failure can lead to catastrophic failure in the specimen or structure. Fiber breakage will be the first of the fiber failures discussed, caused primarily by tensile loads exceeding the strength of the fiber. Once a fiber suffers a breakage, the stress must be redistributed to neighboring fibers and stress redistribution can cause a repeating effect on the neighboring fibers, eventually leading to complete failure of the specimen. From mechanical testing, it can be observed that cracks found in adjacent off-axis plies can affect fiber breakage [7].

Under compressive loads fiber micro-bucking is the main damage mode observed. Fiber micro-buckling was first reported in literature by Argon [10] and is the primary damage mechanism triggered by compressive loads that leads to fiber kinking. The micro-buckling was found to form a kinking band, initiated by fiber misalignment due to the manufacturing processes [4,11]. At the kinking band, shear stresses begin to develop which eventually leads to the buckling of the fiber defined by two modes, shear and extensional. The shear failure is deemed to be the most dominant failure mechanism in fibers [12].
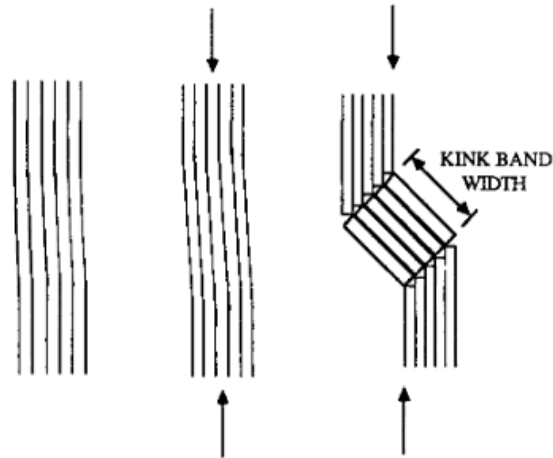
Figure 1.3 Formation of the kinking band in composites [13]

1.3 Continuum and Discrete Damage Mechanics

Damage mechanics is the study and predication of damage initiation and propagation and two main mechanics models have been used in the study of composites, continuum and discrete damage mechanics. Each damage mechanics model comes with both advantages and disadvantages; however, both are used extensively today.

1.3.1 Continuum Damage Mechanics

Continuum Damage Mechanics, CDM, was first formulated by Kachanov in 1958 in the investigation of creep in materials [5,14,15]. However, since then, CDM has advanced in damage mechanics. The main premise of CDM is observing the damage of a material in a variety of damage variables, at first as a scalar value and then progressions to tensors in later developments. Damage accumulation in composites, such as matrix cracks and fiber breakage, are not modeled directly, and, instead, the damage is incorporated into the reduction in stiffness of the specimen. Subsequently, the damage variables involved in CDM model makes it easy for implementation into modern day analysis. An in-depth CDM analysis of laminate composites

6

can be reviewed by the works of Miamí et. al. and a fatigue approach by Llobet et. al. [5,16,17].

However, a key drawback of this method is complicated methods used to monitor damage

interaction, a major factor in specimen failure.

1.3.2 Discrete Damage Mechanics

Discrete Damage Mechanics aims to address the shortcomings of CDM. Discrete

Damage Mechanics, DDM, directly models the displacement discontinuities and allows for the

interaction of the damage, such as the relationship of delamination and matrix cracks discussed

previously. Camacho and Ortiz originally set the foundation of DDM in the modeling of impact

damage on brittle materials using finite element methods [18]. In the original development of

DDM, cracks were confined to follow the boundaries of the finite elements of the model using a

cohesive zone. However, the DDM methodology has transformed to allow damage propagation

to run through elements using mesh independent finite element techniques, allowing for more

accurate representation and damage interaction. DDM methodologies have been applied in

fatigue loading by Iarve, and is currently used in a standalone software BSAM, the software used

in the analysis of the current work [19].
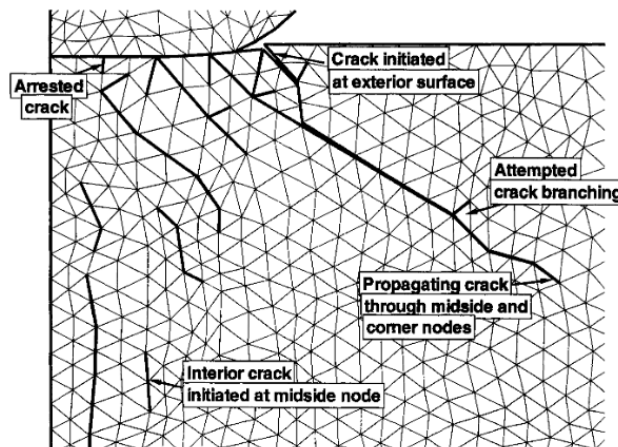
Figure 1.4 Crack propagation using discrete damage mechanics [18]

7

1.4 Finite Element Advancements

After the implementation of DDM into FEA software, several advances in different FE methods were made to increase both computational efficiency and accuracy. In Camacho and Ortiz's first models, a set triangular element mesh was used, only allowing the crack to propagate along element edges, as seen in Figure **1.4**. Three different methodologies using DDM will be introduced, adaptive remeshing, eXtended Finite Element Methods, and the Regularized eXtended Finite Element Method.

1.4.1 Adaptive Remeshing

One of the first advancements involved an adapting remeshing around the crack tip as computation occurs [20–22]. Using adaptive remeshing technique requires the crack path or a pre-crack inserted before computation begins. A fine mesh is found around the crack tip and becomes coarser based on distance from the crack tip. The remeshing then follows an algorithm in which loading occurs, static or fatigue, and a failure criterion is then checked to determine if the crack propagates. After crack propagation, the mesh is refined around the new crack tip and the process is repeated. Adaptive remeshing still was limited to crack propagation along element boundaries, but fine meshes along the crack tip allowed for a more accurate representation of crack propagation in materials. However, the constant remeshing throughout analysis can be computationally taxing and, in the case of laminate composites, surface element connectivity between neighboring laminas can be problematic in delamination studies.
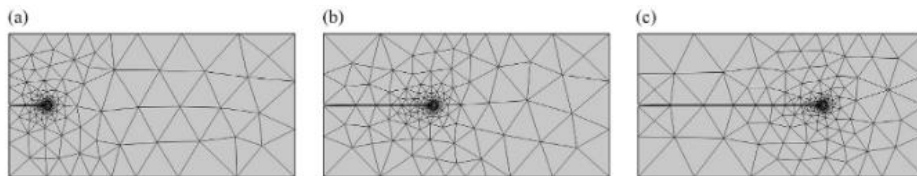
Figure 1.5 Adaptive remeshing technique for crack growth [22]

1.4.2 eXtended Finite Element Method

Researchers looked to fill the flaws of adaptive remeshing techniques by developing the eXtended Finite Element Method, XFEM [23–26]. The basis of XFEM methodologies is nodal enrichment of elements in which the crack or crack tip lies within. A signed distance function is used to determine if arbitrary locations are "above" or "below" the crack, assigning positive and negative values respectively. A Heaviside step function is then deployed to define the displacement jump over the crack, splitting the domain into two separate domains. The classical finite element approach is then slightly changed, adding in the enriched functions to the approach. The issues found in the adaptive remeshing methods are resolved with XFEM, however, XFEM introduces a new issue of having a discontinuous function in the integrand when computing element stiffness, an issue in which the Regularized eXtended Finite Element Method resolves. The mathematical model for XFEM will be discussed in a later chapter.

1.4.3 Regularized eXtended Finite Element Method

To solve the issue of a discontinuous function in the integrand of the stiffness matrix, Iarve proposed replacing the Heaviside step function with a continuous function so that standard Gauss integration can be performed [27]. The computation of displacement discontinuities is then computed the same as XFEM. A further discussion of Regularized eXtended Finite Element Method will be found in the theoretical framework of the current work.

2 Theoretical Framework

The Theoretical Framework chapter is meant to establish the mathematical framework of the current work. Methodologies discussed in the Theoretical Framework provide a heightened knowledge and is pertinent in understanding damage analysis of laminate composites under

fatigue loading. RXFEM and XFEM will be discussed first, providing the foundation of how damage will be modeled in the current work. Following RXFEM and XFEM will be the constitutive model on how crack propagation will occur with an in-depth description of the Cohesive Zone Model. That last two that will be discussed will be Local R-Ratio and fiber failure methodologies incorporated in BSAM. In each section, an emphasis will be put on fatigue formulation for each method.

2.1   XFEM Formulation in Damage Modeling

Before the XFEM and RXFEM methodologies are defined, a background in classic Finite Element Analysis is required and will not be provided in this paper. The reader is directed to the work of Cook et. al. if needed [28]. Although RXFEM is the method used for damage modeling in the current work, some mathematical formation found in XFEM is required before the establishment of RXFEM.

2.1.1   XFEM Formulation of Modeling Cracks

As stated in the Introduction, XFEM looked to address the inability for the classic FEA to model displacement discontinuities in analysis by enriching nodes in elements in which discontinuities are found. XFEM has been used extensively in modeling fracture in composites, including both static and fatigue modeling [29–31]. There can be many formulations of XFEM, however, the methodology chosen is from the book by Mohammadi [26]. The classic FEA displacement field approach is expanded to include the nodal enrichment, found in Equation (2-1) through Equation (2-3).

$$u^h(x) = u^{FE} + u^{enr}$$

(2-1)

10

Where the displacement approximation is broken into its classic u^{FE} and enriched portions u^{enr}. Mohammadi proposes additional terms for the weak formulation; however, the strong formulation will be the focal point.

$$u^{FE} = \sum_{j=1}^{n} N_j(\boldsymbol{x})\boldsymbol{u}_j \qquad (2\text{-}2)$$

$$u^{enr} = \sum_{h=1}^{mh} N_h(\boldsymbol{x})\psi(\boldsymbol{x})\boldsymbol{a}_h + \sum_{k=1}^{mt} N_h(\boldsymbol{x})\left(\sum_{l=1}^{mf} [F_l(\boldsymbol{x}) - F_l(\boldsymbol{x}_k)]\boldsymbol{b}_k^l \right) \qquad (2\text{-}3)$$

The classic FEA displacement approximation is shown in Equation (2-2), where $\mathbf{u}_j$ is the vector of degrees of freedom not enriched and N_j is the corresponding shape functions. In the enriched displacement field term of Equation (2-3), $\mathbf{a}_h$ is the vector of additional degrees of freedom containing the crack interface, N_h is the corresponding shape functions, and ψ is the enrichment functions. The second term contains the additional degrees of freedom containing the crack tip $\boldsymbol{b}_k^l$ and the crack-tip enrichment functions F_l found in Equation (2-4) where r and θ are polar coordinates.

$$F_\alpha(r,\theta) = \left\{ \sqrt{r}\sin\frac{\theta}{2}, \sqrt{r}\cos\frac{\theta}{2},\ \sqrt{r}\sin\theta\sin\frac{\theta}{2}, \sqrt{r}\sin\theta\cos\frac{\theta}{2} \right\} \qquad (2\text{-}4)$$

The number of nodes represented by the classical FEA approach, crack face, and crack tip correlate to n, mh, and mt respectively.

2.1.2 Signed and Jump Step Functions

To determine where elemental nodes are positioned relative to the crack, a signed function is used,

$$\xi(\boldsymbol{x}) = min\|\boldsymbol{x} - \boldsymbol{x}_\Gamma\| sign(\boldsymbol{n} \cdot (\boldsymbol{x} - \boldsymbol{x}_\Gamma)) \qquad (2\text{-}5)$$

where $\mathbf{x}_\Gamma$ is the normal projection of $\mathbf{x}$ on the crack Γ and $\mathbf{n}$ is the unit normal vector. The

distance between any point x to the crack interface is defined as:

$$d = \|\boldsymbol{x} - \boldsymbol{x}_\Gamma\|$$ (2-6)

From the signed function, elemental nodes found "above" the crack are assigned ξ greater than

zero and those found "below" are less than zero. At the crack interface, the signed function is

zero. The sign function allows for a complete model of the crack's geometry in a finite element

model A visual example of a simple domain Ω and the use of the sign function can be found in

Figure **2.1**.
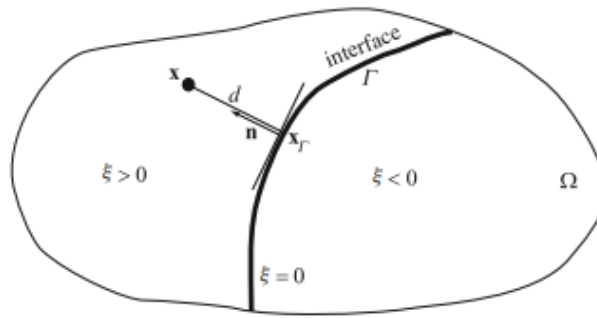
Figure 2.1 Visual representation of the sign function [26]

In the XFEM formulation, the Heaviside step function is used for the enriched function,

shown as ψ in Equation (2-3). The jump function allows for a simple method of modeling the

displacement discontinuity based on the signed function discussed previously.

$$H(\xi) = sign(\xi) = \begin{cases} 1 & \xi > 0 \\ -1 & \xi < 0 \end{cases}$$ (2-7)

2.2 RXFEM Formulation

As stated prior, the XFEM formulation becomes problematic using a discontinuous

function in the integrands of the stiffness matrix. RXFEM follows closely to the XFEM

methodology except for an approximated Heaviside function. The use of a Heaviside

approximation allows enriched function to be continuous, allowing for the integrals in the

stiffness matrix calculation to be carried out by Gauss integration [24,27,32–34].

2.2.1 Regularized Heaviside Function

An approximation for the Heaviside function is defined, using the same shape functions

used in the element force vector and stiffness matrix calculations, as:

$$\widetilde{H}(\xi^e) = \sum_{i \in \Omega_e} N_i^e h_i \tag{2-8}$$

where Ω_e is the set containing all nodes of an element, both enriched and classic, e and ξ are the

parametric coordinates, and N_i^e are the shape functions. Continuity is ensured over the domain

by a single field of nodal values h_i computed for each node, i and summed up over all elements

that share the node.

$$\tilde{h}_i = \frac{1}{2} \left(1 + \frac{\sum_{e \in \mho_i} \int_V N_i^e(\boldsymbol{x}) F(\Gamma) dV}{\sum_{e \in \mho_i} \int_V N_i(\boldsymbol{x}) |F(\Gamma)| dV} \right) \tag{2-9}$$

$\mho_i$ is the set of elements sharing the node of interest and $F(\Gamma)$ is the signed distance function of

the crack surface. The use of the approximated Heaviside function allows for more

computational efficiency than XFEM because of the use of Gauss integration. Multiple cracks in

plies are common, and for each crack Equations (2-8) and (2-9) are used independently for each

crack. Crack surfaces are then defined as Γ_a where the subscript a denotes the crack index. The

signed distance and Heaviside functions then become F_a and $\widetilde{H}_a$ respectively.

2.2.2 Multi-Crack Methodology

RXFEM uses a four-step process in generating the enriched approximation. A simple ten element model will be considered with nodes numbered from 1 to 11, shown in Figure **2.2**(a). A two-crack enrichment is then introduced in Figure **2.2**(b) with the value of the step function for the nodes located in the gradient zone of each crack using a two-digit number scheme.
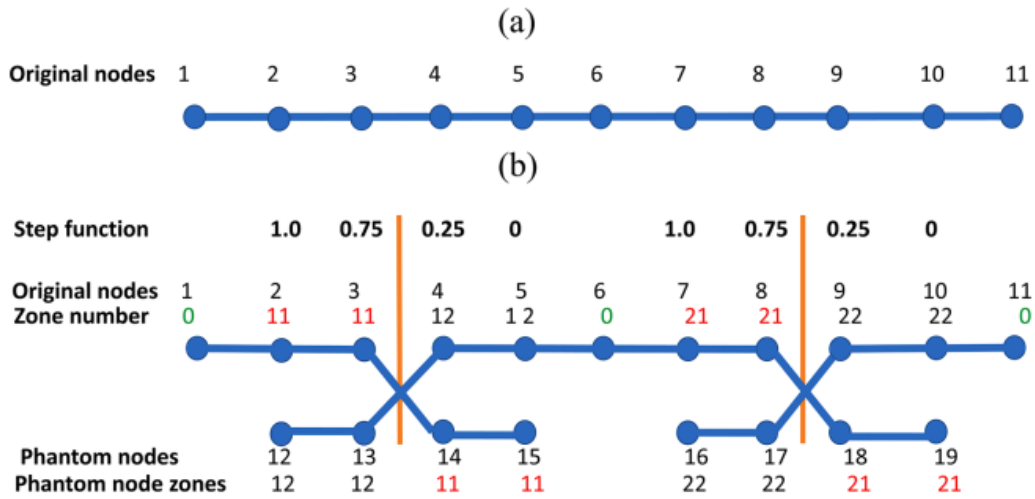
Figure 2.2 (a) Original 1D row of elements (b) enriched node and element set for two cracks [35]

The four steps in generating the enriched approximation first starts with computing the regularized Heaviside function $\widetilde{H}_a$ for each crack using the equations discussed in the previous section. Second, zone numbers are assigned to the original nodes. The first digit represents the crack, 1 or 2, followed by a 1 if $\widetilde{H}_a > 0.5$ or 2 if $\widetilde{H}_a \leq 0.5$. Any nodes outside of the gradient zone are assigned 0. After zoning of the original nodes is complete, original nodes that are in non-zero zones are cloned, and phantom nodes are created that are complementary to the original nodes. This is done by changing the second digit of the original node's zone number to the opposite, such as node 2's zone of 11 to the phantom node's 12 of node 12. The phantom nodes are given unique degrees of freedom and have the initial displacement values of the parent node.

14

Lastly, the enriched element set is created by twinning all elements, so each twinned element contains a combination of original and phantom nodes. The algorithm then collects all nodes, real and phantom, containing the same zone number. During the element twinning process, element twins spatially overlap by layering them under each other, introducing volumetric cohesive forces to tie displacements in the node pairs.

BSAM is used in the current work and allows for much denser crack patterns in the analysis. This is possible by creating no separation between the gradient zones of the cracks as seen in Figure **2.2** by including Node 6. The same four step process established before is followed with a few changes. In Figure **2.3**, Node 5 can be viewed to belong in two zones, for crack one and two, therefore step two of the process assigns two zone numbers to the single node. In step three, Node 5 will contain two phantom nodes, Node 15 and 16, one for each zone. Lastly, twinning of the elements containing original nodes with multiple phantom nodes only happens once, two zones are found for Node 5, 12 and 21. Thus, element 14-15 and 16-17 are deemed zones 11 and 22 respectively.
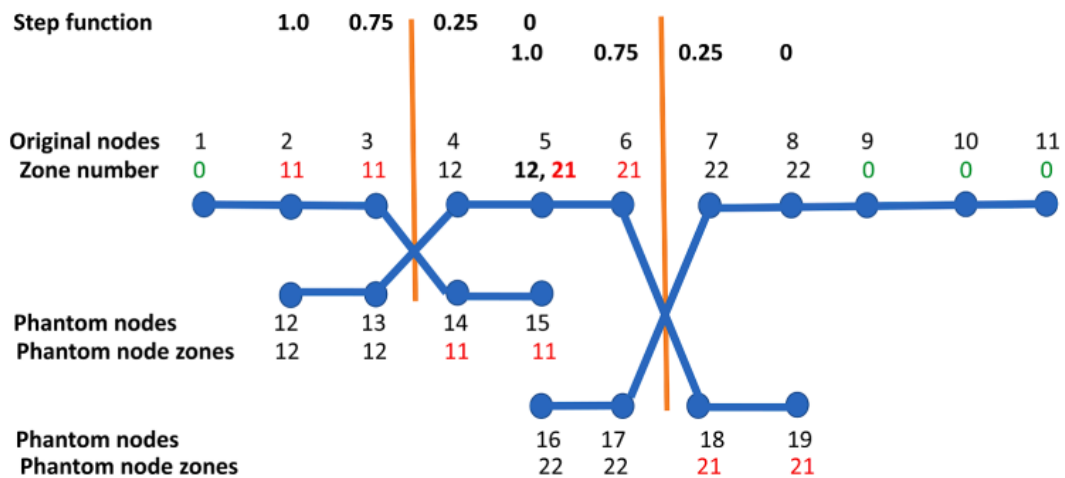
Figure 2.3 Nodal enrichment configuration with no separation between gradient regions of cracks [35]

With nodal enrichment complete, the potential energy Π_n for each cracked ply is

established in Equation (2-10).

$$
\begin{aligned}
\Pi_n = \sum_e \int_{V_e} W(u) + \int_{V_e} \widetilde{H}(F_a)W(u_{a1}) + \int_{V_e} \left(1 - \widetilde{H}(F_a)\right)W(u_{a2})\} \\
- \int_{V_e} |\nabla\widetilde{H}(F_a)| \int_0^\lambda \tau(\lambda)d\lambda\}
\end{aligned}
$$

(2-10)

The summation is performed for all original elements. The first term is only present for

non-twinned elements in zone 0. If the element is twinned, this term is zero and the others are

present. The last term in Equation (2-10) is also integrated over the element volume, yielding the

surface area of the crack from the step function gradient. The displacement fields between

original and phantom nodes u_{a1} and u_{a2} are needed in the Cohesive Zone Model to relate

cohesive tractions τ and displacement jumps λ which will be discussed in a later section. All

functions used are continuous and therefore Gauss quadrature is used. The equilibrium equations

for the laminate are then established in Equation (2-11), where Φ_n is the cohesive traction work

at the interface between plies n and n +1 and A is the work of external forces.

$$
\delta\left(\sum_n^N \Pi_n - \sum_n^{N-1} \Phi_n - A\right) = 0
$$

(2-11)

2.3 Cohesive Zone Model

RXFEM and XFEM methods allow for the modeling of cracks, but how the cracks

propagate is described using the Cohesive Zone Model, CZM. Barenblatt theorized there is a

region just aft of the physical crack tip that is held together by cohesive tractions, the cohesive

zone [36]. In the current era, the CZM approach is one of the most common methods used to

model delamination in laminate composites, relating tractions to displacement jumps, which are easily attainable in a finite element model. The present work will focus on the static formulation by Turon and fatigue formulation by Iarve et. al., relating Fracture Mechanics to Damage Mechanics, which links the Paris Law to a singular damage variable [37–42]. The methodology was chosen as it pertains to high-cycle fatigue, the focus of the current work.

2.3.1 CZM Approach and Kinematics

As stated previously, the CZM model relates tractions to displacement jumps. Damage initiation is based on the interfacial strength and if after plotting the traction versus displacement jump the area under this curve is equal to the fracture toughness of the material, the traction reduces to zero and a new crack surface is formed:

$$\begin{cases} \tau = \left(1 - \bar{d}\right)\tau^o & \bar{\Delta} < \bar{\Delta}^f \\ \tau = 0 & \bar{\Delta} \geq \bar{\Delta}^f \end{cases} \tag{2-12}$$

where τ is the traction, τ^o is the interfacial strength, $\bar{\Delta}$ is the displacement jump, and $\bar{\Delta}^f$ is the final displacement jump. The formulation uses a bilinear relationship between the tractions and the displacement jumps, which gives a linear elastic response before damage initiation. A stiffness parameter K is used to establish a connection between the two surfaces of the damaged region. The stiffness parameter and the interfacial strength then define a displacement jump in which damage is to begin.
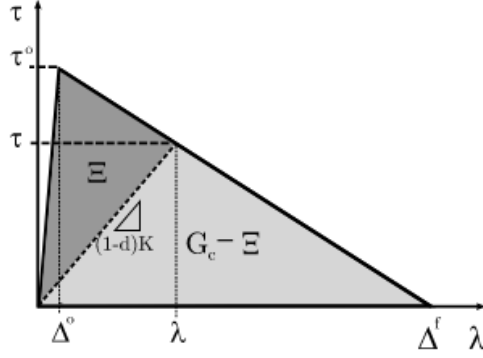
Figure 2.4 Traction versus displacement jump for CZM

The displacement jump is defined as the displacements of points located above and below the discontinuity, in the case of finite elements the nodes or integration points of elements are used.

$$[\![u_i]\!] = u_i^+ - u_i^- \tag{2-13}$$

The displacements used in Equation (2-13) are set in a fixed cartesian coordinate system of the undeformed model where positive and negative superscripts represent the top and bottom points or nodes of the discontinuity, u_i^+ and u_i^-. If the model of interest has been deformed from loading, a new coordinate system $\bar{x}_i$ is introduced:

$$\bar{x}_i = X_i + \frac{1}{2}(u_i^+ + u_i^-)s \tag{2-14}$$

where X_i are the coordinates from the undeformed model. The components of the displacement vector of the undeformed model of Equation (2-13) on the deformed interface are expressed using the displacement field in the global coordinates:

$$\Delta_m = \Theta_{mi}[\![u_i]\!] \tag{2-15}$$

18

where Δ_m are components of the displacement jump vector defined in the coordinates of the deformed interface and Θ_{mi} is the rotational tensor matrix. The displacement vector contains shear and normal components, Δ_1, Δ_2, and Δ_3 respectively.

2.3.2 Traction-Displacement Jump Constitutive Laws

With the approach and kinematics of CZM established, the relationship between the tractions and displacement jump is required. The constitutive law used follows a CDM model using the free energy per unit surface of the interface [43–45]:

$$\psi(\Delta, d) = \psi(\Delta, d)_{coh} + \psi(\Delta, d)_{con} \tag{2-16}$$

where d is the damage variable and ψ is the free energy per unit surface. From Equation (2-16), the right-hand side consists of two components, ψ_{coh} and ψ_{con} being the cohesive and contact energy contributions respectively. The energy contributions are then defined as:

$$\psi(\Delta, d)_{coh} = \frac{1}{2}(1 - d)[\Delta_i K_{ij} \Delta_j - K_{33}\langle -\Delta_3 \rangle^2] \tag{2-17}$$

$$\psi(\Delta, d)_{con} = \frac{1}{2}[K_{33}\langle -\Delta_3 \rangle^2] \tag{2-18}$$

where δ_{i3} is the Kroenecker delta, K_{ij} are elements of the stiffness matrix with K_{33} being the penalty stiffness for Mode I and K_{22} and K_{33} for the shear modes, and $\langle \cdot \rangle$ is the MacAuley bracket. With the free energy equations established, the constitutive equation between tractions and displacement jumps is written as:

$$\tau_i = \frac{\partial \psi}{\partial \Delta_i} = D_{ij} \Delta_j \tag{2-19}$$

where D_{ij} is the constitutive tensor:

19

$$D_{ij} = (1 - d)K_{ij}\Delta_j + d\delta_{i3}K_{33}\langle-\Delta_3\rangle \quad (i,j = 1,2 \; or \; 3) \tag{2-20}$$

From the resulting constitutive relationship, one can see that only the cohesive component contributes to the formulation of Equation (2-19). Therefore, only cohesive tractions will be considered. A norm for the mixed-mode traction τ and displacement jumps λ are defined to proceed in formulating the damage evolution law:

$$\tau = \sqrt{\tau_1^2 + \tau_2^2 + \langle\tau_3\rangle^2} = (1 - d)K_B\lambda \tag{2-21}$$

where K_B is a mode-dependent penalty stiffness:

$$K_B = \frac{K_{11}^2\Delta_1^2 + K_{22}^2\Delta_2^2 + K_{33}^2\langle\Delta_3\rangle^2}{K_{11}\Delta_1^2 + K_{22}\Delta_2^2 + K_{33}\langle\Delta_3\rangle^2} \tag{2-22}$$

Using Equation (2-21) and a relationship between the cohesive free energy, equivalent traction, and equivalent displacement jump, a formulation of the displacement jump norm is defined:

$$\psi_{coh} = \frac{1}{2}\tau\lambda \tag{2-23}$$

$$\lambda = \frac{K_{11}\Delta_1^2 + K_{22}\Delta_2^2 + K_{33}\langle\Delta_3\rangle^2}{\sqrt{K_{11}^2\Delta_1^2 + K_{22}^2\Delta_2^2 + K_{33}^2\langle\Delta_3\rangle^2}} \tag{2-24}$$

A local mixed mode ration B is defined using the energy release rate, ERR, for each mode:

$$B = \frac{G_1 + G_2}{G} \tag{2-25}$$

where G_1 and G_2 is the ERR for each mode and G is the total ERR.

$$G_i = \int_0^{\Delta t} \tau_i d\Delta_i \tag{2-26}$$

$$G = \int_0^{\lambda} \tau d\lambda \tag{2-27}$$

Using the previously defined displacement jump norm and mode-dependent penalty stiffness, the mixed-mode ratio can also be defined as:

$$B = \frac{K_{11}\Delta_1^2 + K_{22}\Delta_2^2}{K_{11}\Delta_1^2 + K_{22}\Delta_2^2 + K_{33}\langle\Delta_3\rangle^2} \tag{2-28}$$

Lastly, the mode-dependent stiffness can be reduced using the new definition of the mixed-mode ratio and defining $K_{sh} = K_{11} = K_{22}$.

$$K_B = K_{33}(1 - B) + BK_{sh} \tag{2-29}$$

2.3.3 Fatigue CZM Formulation

The current work focuses on damage evolution under fatigue loading, therefor, the fatigue formulation is emphasized. For the fatigue formulation, a focus will be put on the work of Iarve et. al., a modified CZM methodology replacing the static strength Y with residual strength [42,46]. First, the initial Δ_0 and final displacement jump Δ_c in the static region is defined as:

$$\Delta_0 = \frac{Y}{K} \tag{2-30}$$

$$\Delta_c = \frac{2G_c}{Y} \tag{2-31}$$

where G_c is the critical ERR and K is the penalty stiffness of Equation (2-29). The fatigue loading amplitude f where the material point is in the initiation phase is assumed to be:

$$f = \frac{\lambda_0}{\Delta_0} \tag{2-32}$$

As stated previously, the basis of the fatigue formulation is the changing of the static strength, using the strength tracking method, with the residual strength through analysis, such that:

$$f_{r''}Y < f_{r'}Y < Y \tag{2-33}$$

The residual strength factor $f_{r''}$ is calculated by:

$$\frac{1}{N_{lim}(f_{r''})} = \frac{1}{N_{lim}(f_{r'})} + \frac{\Delta N}{N_{lim}(f)} \tag{2-34}$$

where N_{lim} is the number of cycles at which failure is reached, a function of the residual strength factor, and ΔN is the number of cycles between each step.

At some point in the fatigue analysis $f \geq f_r$ where the damage regime of CZM begins and the static strength is replaced with the residual strength Y_r.

$$Y_r = f_r Y \tag{2-35}$$

The displacement jumps of the static regime are then replaced with their fatigue counterparts λ_0 and λ_c:

$$\lambda_0 = \frac{Y_r}{K} \tag{2-36}$$

$$\lambda_c = \frac{2G_c}{Y_r} \tag{2-37}$$

A new damage norm is then established, RT:

$$RT = \frac{\lambda - \lambda_0}{\lambda_c - \lambda_0}$$ (2-38)

where the displacement jump λ is the same as described in Turon's formulation of Equation

(2-24). The damage norm then defines the damage variable as:

$$D = \frac{RT\lambda_c}{RT\lambda_c + (1 - RT)\lambda_0}$$ (2-39)

Figure **2.5** shows a graphical depiction of the fatigue damage initiation for CZM.
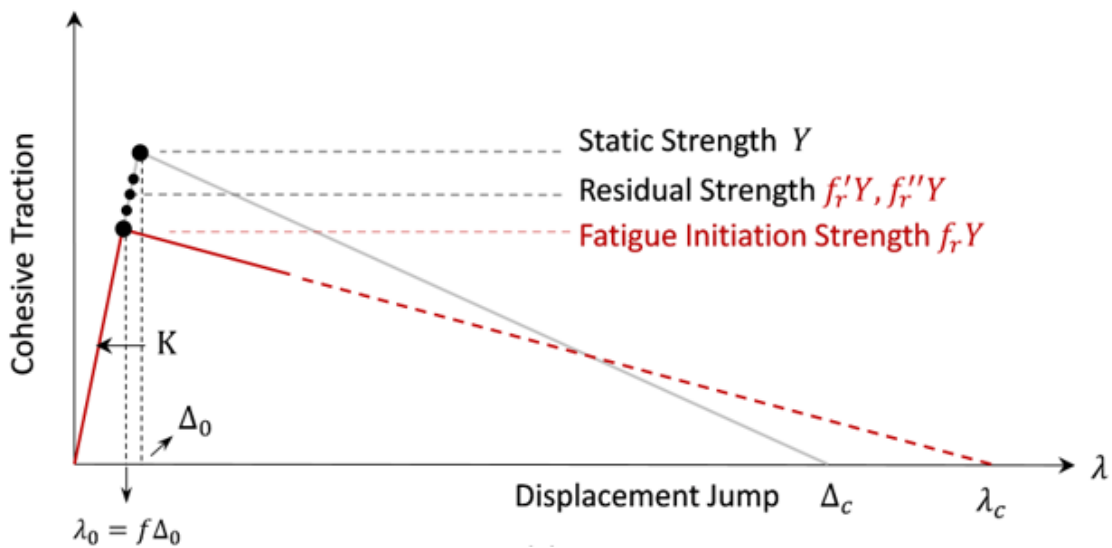
Figure 2.5 Cohesive-Displacement jump model for fatigue damage initiation [35]

2.3.4   Fatigue Damage Propagation

The Paris Law has been commonly used for crack propagation in laminate composites

and has been proposed in a variety of forms [47,48]. The law, first proposed by Paris, aims to

create a relationship between crack propagation rates with stress intensity factors [49]. The

current work will focus on the modified Paris Law found in the formulation by Tao et. al. [50],

which follows closely to the stress intensity factor formulation but with the use of ERR:

23

$$\frac{da}{dN} = C\left(\frac{\sqrt{G_{max}}}{\sqrt{G_c}} - \frac{\sqrt{G_{min}}}{\sqrt{G_c}}\right)^{2m} \tag{2-40}$$

where G_{max}, G_{min}, and G_c are the maximum, minimum, and critical ERR during the cycle. C and m are material constants obtained through mechanical testing and depend on the mode mixity of Equation (2-28). The ERR is calculated based on the area under the curve of the traction-displacement curve, mathematically represented in Equation (2-27).

First, we will consider an initial displacement jump of λ_1 corresponding to a material point in the damage phase with a damage variable D_1. Calculation of the ERR from Equation (2-27), the ERR is defined as:

$$G_{max}^{[1]} = \frac{1}{2}[Y_r\lambda_1 + K(1 - D_1)\lambda_1(\lambda_1 - \lambda_0)] \tag{2-41}$$

Now another displacement jump λ_2 with a designated damage variable D_2 is examined after a number of fatigue cycles. A graphical depiction of this jump can be found in Figure **2.6**. The ERR is calculated by adding the area under the traction-displacement jump curve between λ_1 and λ_2 and the ERR found in the first calculation of Equation (2-41):

$$G_{max}^{[2]} = G_{max}^{[1]} + \frac{1}{2}[(K(1 - D_1)\lambda_1 + K(1 - D_2)\lambda_2)(\lambda_2 - \lambda_1)] \tag{2-42}$$

Once the maximum ERR is obtained, the minimum ERR is found through the relationship between the fatigue stress ratio, R, and the maximum ERR:

$$G_{min} = R^2 G_{max} \tag{2-43}$$

Using Equation (2-40), the crack propagation rate can be calculated for each integration point located in the element. The propagation rate in the element is determined by the maximum propagation rate found in all integration points in the element:

$$E_p = \max\left[C\left(\frac{\sqrt{G_{max,i}}}{\sqrt{G_c}} - \frac{\sqrt{G_{min,i}}}{\sqrt{G_c}}\right)^{2m}\right] \tag{2-44}$$

where i is each integration point in the element.
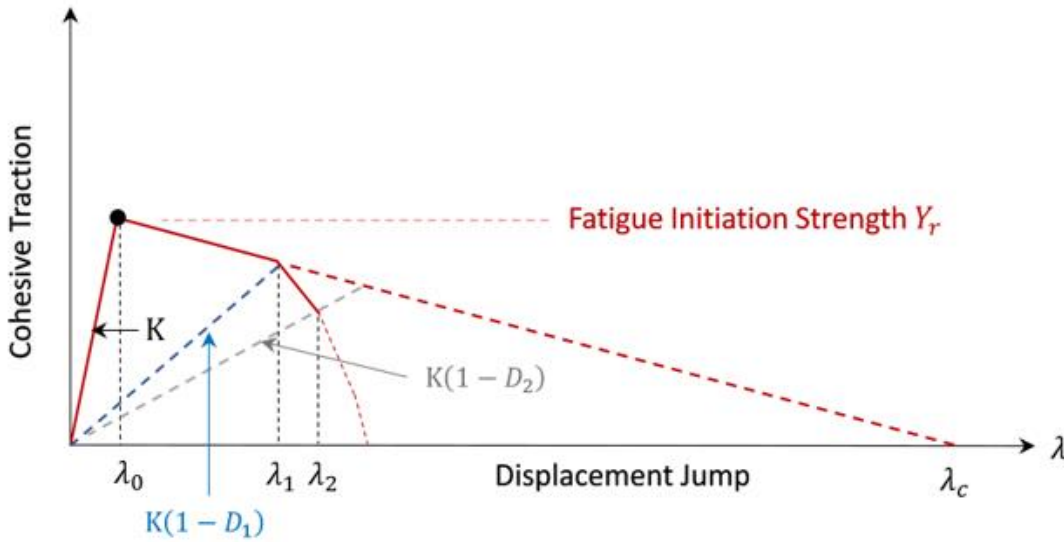
Figure 2.6 Cohesive-Displacement jump model for fatigue damage propagation [35]

To calculate the number of cycles for a crack to propagate through the entire element, an element effective length is established from the basis of Tao et. al. and the reader is directed there for the mathematical formulation [50]. The effective length, defined in the current paper as l_e, is a characteristic length that establishes the length of a crack or delamination needs to propagate for a local element to be considered to have failed and is always in the direction of crack or delamination propagation. With the element effective length established, the cycle increment needed to propagate the crack through the element can be defined ΔN_p:

$$\Delta N_p = l_e / E_p \qquad\qquad (2\text{-}45)$$

Now that the cycle increment needed for the crack to propagate through an entire element, the algorithm can update the damage norm of Equation (2-38):

$$RT_f^u = RT + (1 - RT)\frac{\Delta N}{\Delta N_p} \qquad\qquad (2\text{-}46)$$

where ΔN is the cycle increment in an analysis step, u superscript denotes update, and f subscript denotes fatigue. However, in the algorithm the damage norm is updated based on the maximum value of both the static and fatigue regime.

$$RT^u = \max\left(RT, RT_f^u\right) \qquad\qquad (2\text{-}47)$$

Elements in a finite element model are often not all the same size or shape. Therefore, the effective length of each element can differ, causing the increment of cycles for the crack or delamination to go through each element is different. This observation affects the fatigue damage norm updating of Equation (2-46) to be different across different elements in the model.

2.4 Fiber Failure in Compression

As the current work involves methodologies that have expanded into compression-compression and compression-tension validation, the establishment of fiber failure methodology is pertinent. The first mechanical model was developed by Argon, but the chosen methodology is based on the fiber misalignment concept by Rosen, which was further refined and implemented into a computation framework by a NASA lead effort resulting in a series of failure criteria LaRC03, LaRC04, LaRC05 [51–53]. According to this concept, a certain misalignment of fibers inevitably present in composite plies gives rise to shear stresses even if a pure unidirectional fiber direction compression is applied. The compression failure takes place when such shear

stresses exceed the shear strength of the material and, in the presence of nonlinear shear, when the matrix softens so much that it cannot sustain fiber rotation. At this point, a small increase in load will cause a drastic angle change, forming the kink band and leading to fiber failure. In the introduction, it was said that compression loading forms a kinking band occurred from micro-buckling of the fibers. In this kink-band region, stresses endured must be transformed from the global coordinate frame into a new local coordinate frame for the misaligned region, where the rotation angle is defined as $\theta = \gamma_{12}^m + \theta_i$ and γ_{12}^m is the shear strain in the misalignment frame and θ_i is the initial misalignment angle.
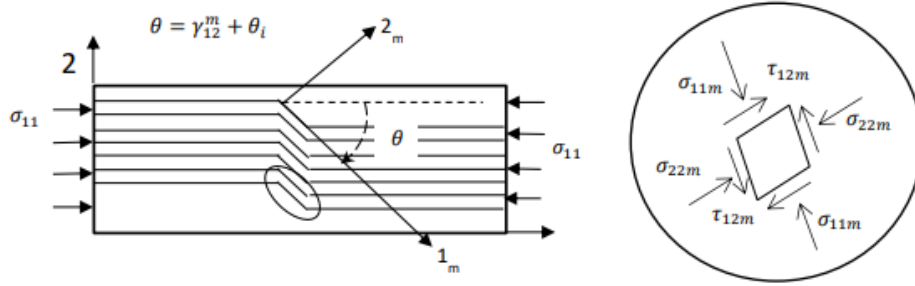

Figure 2.7 Fiber kink-band orientation [12]

2.4.1 BSAM Model

The fiber failure model implemented in BSAM is based in LaRC04 failure criterion. The stresses found in the misalignment frame are as follows where σ_{11}^m, σ_{22}^m, and τ_{12}^m are the longitudinal, transverse, and shear stresses.

$$\sigma_{11}^m = \frac{\sigma_{11} + \sigma_{22}}{2} + \frac{\sigma_{11} - \sigma_{22}}{2} cos(2\theta) + \tau_{12} sin (2\theta) \tag{2-48}$$

$$\sigma_{22}^m = \frac{\sigma_{11} + \sigma_{22}}{2} - \frac{\sigma_{11} - \sigma_{22}}{2} cos(2\theta) - \tau_{12} sin (2\theta) \tag{2-49}$$

$$\tau_{12}^m = -\frac{\sigma_{11} - \sigma_{22}}{2} \sin(2\theta) + \tau_{12}\cos(2\theta) \tag{2-50}$$

For failure under pure compression ($\sigma_{11} = -X^C$ and $\sigma_{22} = \tau_{12} = 0$), Equations (2-48)-(2-50) are reduced to the following with X^C being the compressive strength:

$$\sigma_{11}^m = -X^C \cos^2 \theta \tag{2-51}$$

$$\sigma_{22}^m = X^C \sin^2 \theta \tag{2-52}$$

$$\tau_{12}^m = X^C \sin(\theta) \cos(\theta) \tag{2-53}$$

Using the stress state, one can find the specific misalignment angle that would lead to failure under pure compression. This angle is defined θ^c. Failure from kinking in pure compression because of matrix failure is defined using the LaRC04 matrix compression failure criterion. Equation (2-54) can then be rearranged to find the critical misalignment angle where S^L is the shear strength and η^L is a friction coefficient.

$$X^C (\sin \theta^c \cos \theta^c - \eta^L \sin^2 \theta^c) = S^L \tag{2-54}$$

$$\theta^c = \arctan\left(\frac{1 - \sqrt{1 - 4\left(\frac{S^L}{X^C} + \eta^L\right)\frac{S^L}{X^C}}}{2\left(\frac{S^L}{X^C} + \eta^L\right)}\right) \tag{2-55}$$

Equation (2-54) is the basis of determining fiber failure in BSAM. Once the shear stress developed in the kink band from axial compressive stresses reaches the shear strength of the matrix, fiber failure is to occur as the matrix is unable to support the fibers. The compression failure takes place when the fiber rotation due to initial misalignment angle and applied shear becomes θ^c, i.e. $\theta^c = \gamma_{12}^{m,c} + \theta_i$. The critical value of shear strain can be obtained from shear stress in the misalignment frame Equation (2-56) and the stress-strain constitutive relationship.

$$\tau_{12}^m = f_{CL}(\gamma_{12}^m) \tag{2-56}$$

$$\gamma_{12}^{m,c} = f_{CL}^{-1}(\frac{1}{2}\sin(2\theta^c)\,X^C) \tag{2-57}$$

In the current work, linear shear and small angle approximations is considered, reducing Equation (2-57) to the following:

$$\gamma_{12}^{m,c} = \frac{\theta^c X^C}{G_{12}} \tag{2-58}$$

where G_{12} is the shear modulus. Which allows to calculate the initial misalignment angle:

$$\theta_i = \theta^c - \gamma_{12}^{m,c} \tag{2-59}$$

The failure initiation indicator F_{if} is defined as the ratio of the shear stress to respective strength in the misalignment frame, i.e.

$$F_{if} = \frac{\tau_{12}^m}{S_L} \tag{2-60}$$

Where the misalignment angle in Equation (2-59) is a function of the shear stress. In the case of linear stress-strain shear relation and small angle rotation the misalignment angle can be approximated as:

$$\theta = \frac{\theta_i G_{12} + |\tau_{12}|}{G_{12} + \sigma_{11} - \sigma_{22}} \tag{2-61}$$

In this case the F_{if} can be calculated by substituting Equation (2-61) in Equation (2-50) and subsequently in Equation (2-60). It is worth mentioning that in the case of linear shear constitutive equation and uniaxial loading the failure initiation factor Equation (2-60) simplifies

to $F_{if} \cong -\sigma_{11}/X_c$, under assumptions that the strength magnitude is much smaller than the elastic modulus and the rotation angles are small as well.

The failure initiation factor $F_{if} > 1$ corresponds to damage initiation, which for the fiber failure mode is modeled by CDM and a single damage variable property degradation model is used.

$$C = (1 - d)C_0 \tag{2-62}$$

The damage variable d becomes positive when $F_{if} > 1$ and is calculated according to the tri-linear relationship introduced in Maimi et al [54]. C_0 is the stiffness tensor of the pristine material. The reader is referred to Hoos et al. for details [55]. In a simplified case of a bi-linear failure envelope the damage variable is defined as

$$d = \frac{q(F_{if} - 1)}{F_{if}(q - 1)}, q \geq F_{if} \geq 1 \tag{2-63}$$

where

$$q = \frac{2G_{xc}E}{L_e X_c^2} \tag{2-64}$$

for compression loading case. Similar expression is used in tension by replacing the respective strength and fracture toughness values. The finite element size L_e is required for reducing the mesh dependence of the smeared crack model in CDM.

2.4.2 BSAM Fatigue Damage Model for Fiber Failure

The fiber direction damage modeling under fatigue loading, and the compression failure fatigue, is based on application of the strength tracking method and CZM envelope modification

like discussed in the section 2.3.3. The strength tracking method is directly applied to recalculate the shear strength in Equation (2-60) after each cycle increment. In this case, the load amplitude is $f = F_{if}$ instead of Equation (2-32) and the Equations (2-33)-(2-35) apply without change for calculating the load reduction factor f_r, where the strength Y is replaced by shear strength S_L. The $N_{\lim}$ is calculated by using the shear strength S-N curves. The reduced shear strength $S_L' = f S_L$ is then applied to calculate new $F_{if}' > F_{if}$ in Equation (2-60). Thus, the failure initiation indicator will grow with each cycle increment even if the stress σ_{11} remains constant. In the proposed empirical fatigue model, the fiber failure envelope is modified similar to the CZM envelope in Figure 2.5 so that the strength value is reduces to $X_c' = f X_c$, however, besides that modification the area of the envelope is also proportionally reduced so that $G_{xc}' = f^2 G_{xc}$. As a result, the stiffness reduction damage variable d under fatigue loading is calculated by replacing F_{if} with F_{if}' in Equation (2-63), whereas the value of q does not change. It is seen that for $q > 1$ and $F_{if} > 1$ the damage variable d is in an increasing function of F_{if}. In the case of tri-linear failure envelope the principal behavior is the same.

2.4.3 Multi-Damage Variable Model

Recently a physics-based compression fatigue model based on multi damage variable static model explained in by Hossain [12]. The reference model uses five damage variables, $d_{1+}, d_{1-}, d_{2+}, d_{2-}$, and d_{6s}, related to fiber direction failure, transverse direction failure, and shear degradation. The conceptual model behind the fiber direction compression damage variable d_{1-} definition is like described above. However, the model utilizes non-linear stress strain definition

$$\gamma_{12}^m = \frac{\tilde{\tau}_{12}^m}{G_{12}} + \left(\frac{\tilde{\tau}_{12}^m}{K_{12}}\right)^{\frac{1}{n_{12}}} \tag{2-65}$$

In addition, it considers permanent plastic strain γ^p accumulated during cyclic loading. This strain contributes to increasing the rotation misalignment angle so that the rotation angle is

$$\theta = \gamma_{12}^m + \theta_i + \gamma^p \tag{2-66}$$

Thus, an additional mechanism contributing to the kink band formation is considered. Calculation of the permanent cyclic plastic strain requires additional input data not available for the material at hand.

2.4.4 Local Stress Ratio

During fatigue loading, the applied stress ratio, ratio of minimum to maximum stress, is not the stress ratio found throughout the entire model, instead, a local stress ratio is defined. A local stress ratio is observed because of a variety of reasons such as residual stresses and the application of several loads on the specimen at once which can cause different rates of damage propagation through the model than taking the general applied stress ratio [56,57]. There have been several proposed methods in calculating the local stress ratio such as the minimum-maximum load and cycle jump approaches [58,59]. However, the methodology chosen in the present work is developed by Lu et. al. and is implemented in the BSAM analysis software.

The basis of the chosen methodology is monitoring the ERR during the loading and unloading of the model. At certain observation points, the ERR is noted and after the reloading is complete, the maximum and minimum ERR is calculated.
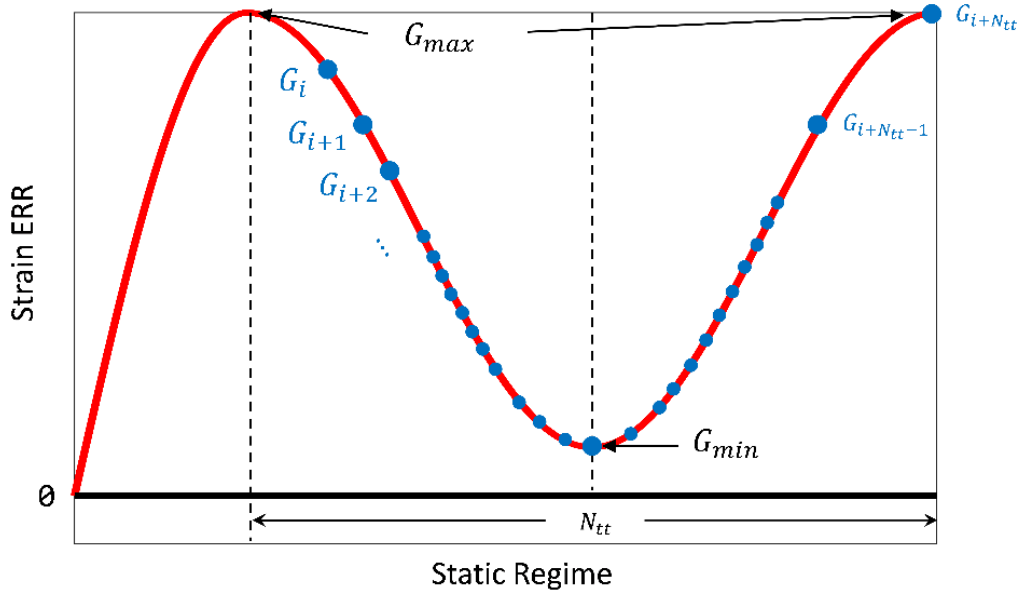
Figure 2.8 Tension-Tension loading and unloading ERR recording

Figure **2.8** presents the loading and unloading process for a tension-tension test where $i +$ n subscripts denote observation points during the test and N_{tt} is the total steps for the complete loading and unloading cycle. After the maximum and minimum ERR is found from the loading/unloading, the local stress ratio is obtained by Equation (2-43) and the damage variables are updated using the local stress ratio. The same process can be using for compression-tension loading as in Figure **2.9**. N^- are the total steps when the model is subject to negative shear loading and N^+ is the total steps where the model is reloaded back with positive shear. The ERR is always positive in both loading scenarios and R-ratios are assumed to be zero in both the positive and negative region.
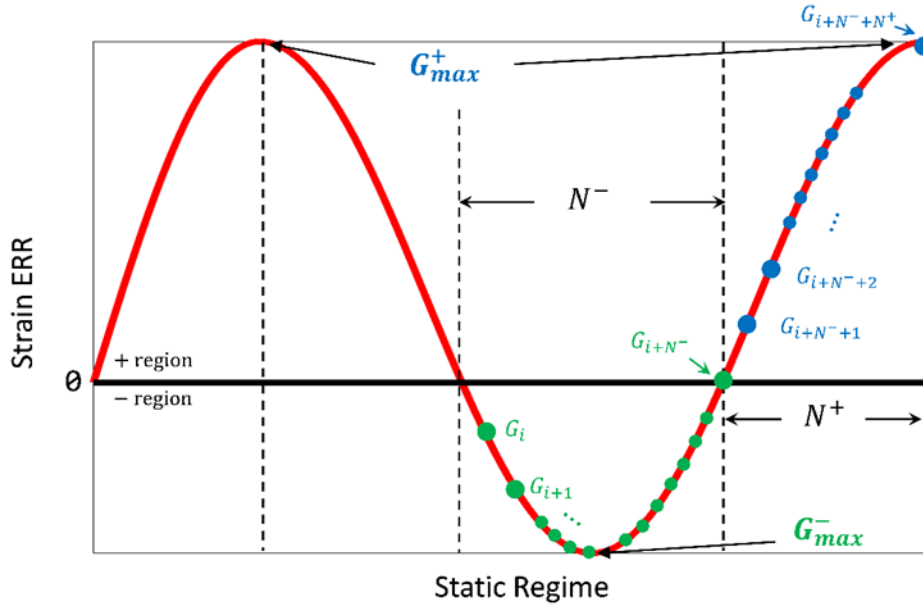
Figure 2.9 Compression-Tension loading and unloading ERR recording

With local R-ratio data collected, S-N parameters are modified based on the methodology by Dávila [60]. The allowable stress σ_{eR} is defined as:

$$\sigma_{eR} = \frac{C_L \sigma_c}{2 - R} \tag{2-67}$$

where σ_c is the ultimate stress and C_L is the load correction factor for the endurance limit.

$$C_L = 1 - 0.42B \tag{2-68}$$

The S-N relationship is defined:

$$\frac{\sigma_{eR}}{\sigma_c} = 1 - sLog_{10}(N) \tag{2-69}$$

where the s coefficient is dependent on the shear and normal stress combination. The new S-N parameters s^n based on old s^o parameters and the new and old stress ratios for mode I and mode II fatigue are defined.

$$s_I^n = s_I^o \frac{(1 - R_n)(2 - R_0)}{(1 - R_0)(2 - R_n)} \qquad (2\text{-}70)$$

$$s_{II}^n = s_{II}^o \frac{(1.42 - R_n)(2 - R_0)}{(1.42 - R_0)(2 - R_n)} \qquad (2\text{-}71)$$

2.5 Methodology Verification

Since RXFEM and CZM is the chosen FE methodology for modeling damage of composites in BSAM, it is important to perform validation studies to ensure it can accurately represent fatigue damage and show the damage interaction between matrix cracks and delamination. Although the current work focuses on open hole models, it is important to ensure the theory is applicable at the most basic level, therefore, double cantilever beam and end notched flexure models are first considered. The verification is then moved over to the three Open Hole Tension-Tension, OHT-T, specimens each using different layups to demonstrate accurate predictions by the methodologies [42].

2.5.1 Double Cantilever Beam

The Double Cantilever Beam, DCB, model is one of the most basic experimental tests performed on laminate composites to observe delamination between laminates caused by mode 1 loading [61]. An FEA model of IM7/8552, material properties can be found in Table 1, is created by modeling a two-ply composite that is 206.1 mm long, 25.4 mm wide, and 2.286 mm thick. The interface between the two plies contains a pre-inserted crack and a bonded region. An edge of the lower and upper ply at the negative x-axis face is then displaced in the z-direction by -1.5 mm ($u_z = -1.5$) and 1.5 mm ($u_z = 1.5$) respectively. After the static loading is complete, a fatigue

analysis is performed. The model is post-processed using the methods by Dávila, obtaining the

ERR and crack growth [60]. The results are then plotted against the true material's Paris Law,

seen in Figure **2.10**.

Table 1 IM7/8552-1 Material Properties

Property	Value	Unit
E_{11}	157.2	GPa
E_{22}, E_{33}	9.38	GPa
G_{12}, G_{13}	5.03	GPa
G_{23}	3.24	GPa
v_{12}, v_{13}	0.30	
v_{23}	0.496	
α_1	0.00	
α_2	30.0 E – 6	1/C
G_{IC}	0.256	N/mm
G_{IIC}	0.649	N/mm
Y_T	81.0	MPa
Y_C	312.0	MPa
S	133.8	MPa
X_T	2490	MPa
X_C	1990	MPa
S_1	0.026	
S_2	0.071	
m_1	12.39	
m_2	5.49	
C_1	0.0055	mm
C_2	0.305	mm
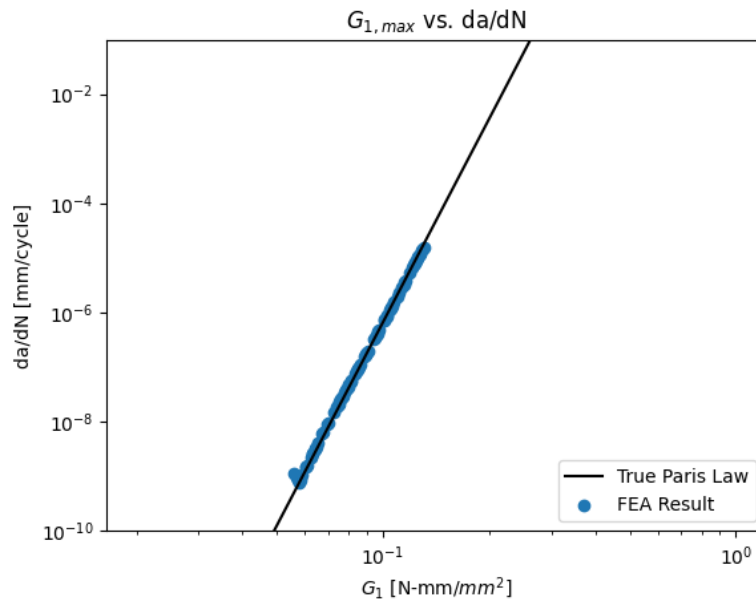
Figure 2.10 Paris Law results from DCB model of IM7/8552-1

From the results, the crack propagation follows very closely to the true Paris Law curve obtained through mechanically testing the material. Confirming that the CZM methodology implemented in BSAM is accurate for validating fatigue results obtained experimentally.

2.5.2 End Notched Flexure

The second methodology verification was performed on an end notched flexure (ENF) model, ensuring that damage propagation from mode 2 loading can be modeled. For the verification, IM7/8552-1 was once again used. The model used is 203.2 mm long, 25.4 mm wide and consists of two plies with thicknesses of 1.905 mm. Two rollers are placed 23 mm and 180 mm from the left edge of the bottom ply. A 53 mm crack is pre-inserted between the interface of the two plies. Static loading begins by applying a -2.97 mm displacement (u_z = -2.97), corresponding to 60% of the ultimate stress, through the width at 101.6 mm of the top ply. After static loading, fatigue loading is started. After the simulation is complete, post processing is performed, calculating the ERR and crack growth once again. The computational results are then

plotted against the true mode II Paris Law in Figure **2.11**. From the results, the crack growth

follows very closely to the true Paris Law function, except for a few outlier data points that can

be determined to be in region 1 of the Paris Law, where crack propagation is not yet linear, and

the cohesive zone is forming.
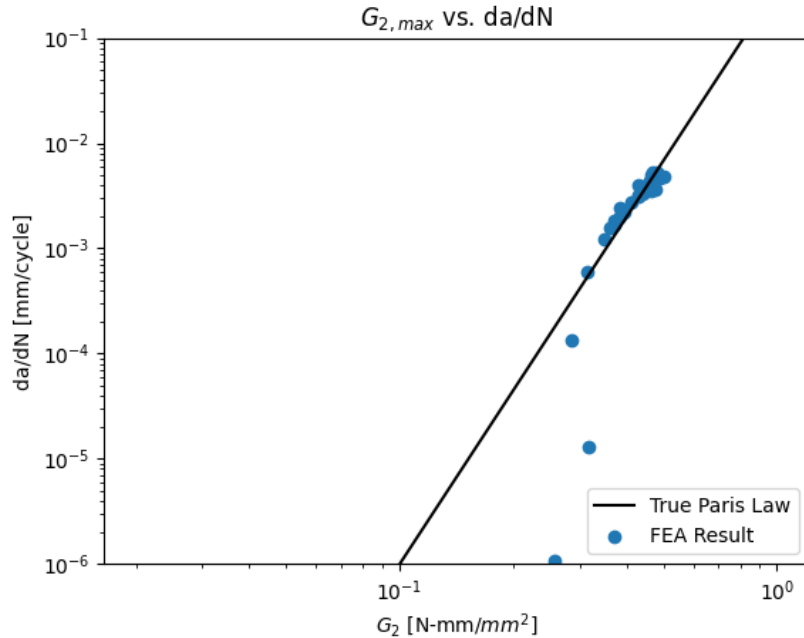
Figure 2.11 Paris Law results from ENF model of IM7/8552-1

2.5.3 Open Hole Tension

The material used in all three specimens is IM7/977-3 with stacking sequences

$[30°/60°/90°/-60°/-30°]_s$, $[0°/45°/90°/-45°]_{2s}$, and $[60°/0°/-60°]_{3s}$. The dimensions

of the specimens are 250 mm long, 38.1 mm wide, and have a 6.35 mm hole in the center. For

the analysis, the left edge of the specimens is constrained in the *x*-direction, $u_x = 0$, while a

loading tab is attached on the right edge. A uniform stress is applied to the right side of the tab

based on a percentage of the failure force divided by the laminate's side area found in static

testing. A fatigue simulation is then performed in BSAM and the results are then compared with

x-ray images of the experiment. The material properties of IM7/977-3 is found in Table 2 and the

fatigue analysis compared with the experimental results are in the following figures.

Table 2 Material Properties of IM7/977-3 [42]

Property	Value	Unit
E_{11}	164.0	GPa
E_{22}, E_{33}	8.97	GPa
G_{12}, G_{13}	5.02 (NLS)	GPa
G_{23}	3.00	GPa
v_{12}, v_{13}	0.32	
v_{23}	0.496	
α_1	0.00	
α_2	30.0 E – 6	1/C
G_{IC}	0.256	N/mm
G_{IIC}	0.649	N/mm
Y_T	100.0	MPa
Y_C	247.0	MPa
S	100.0	MPa
X_T	2900	MPa
X_C	1680	MPa
S_1	0.03	
S_2	0.075	
m_1	7.32	
m_2	6.354	
C_1	0.025	mm
C_2	0.065	mm
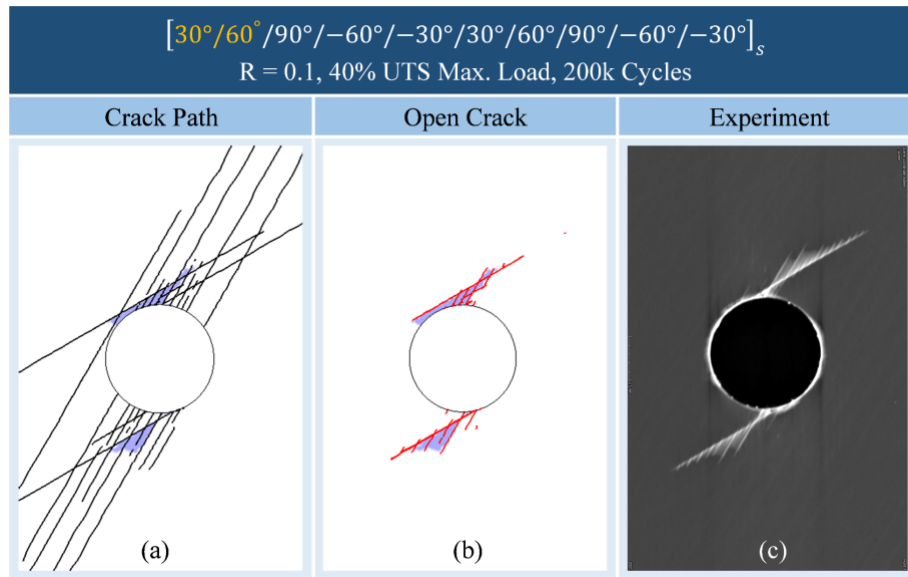
Figure 2.12 Matrix cracks and delamination between 30° and 60° plies of the $[30°/60°/90°/-60°/-30°]_s$ layup at

200k cycles
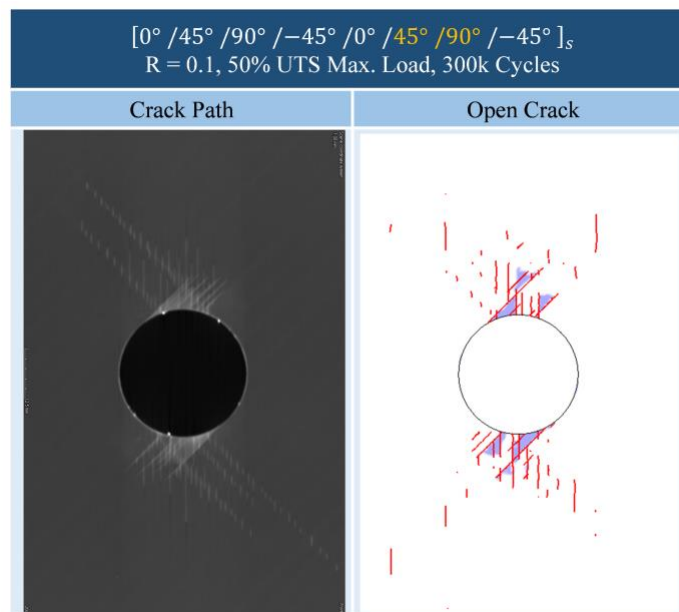
Figure 2.13 Matrix cracks and delamination at the inner 45° and 90° plies of the $[0°/45°/90°/-45°]_{2s}$ layup at
300k cycles
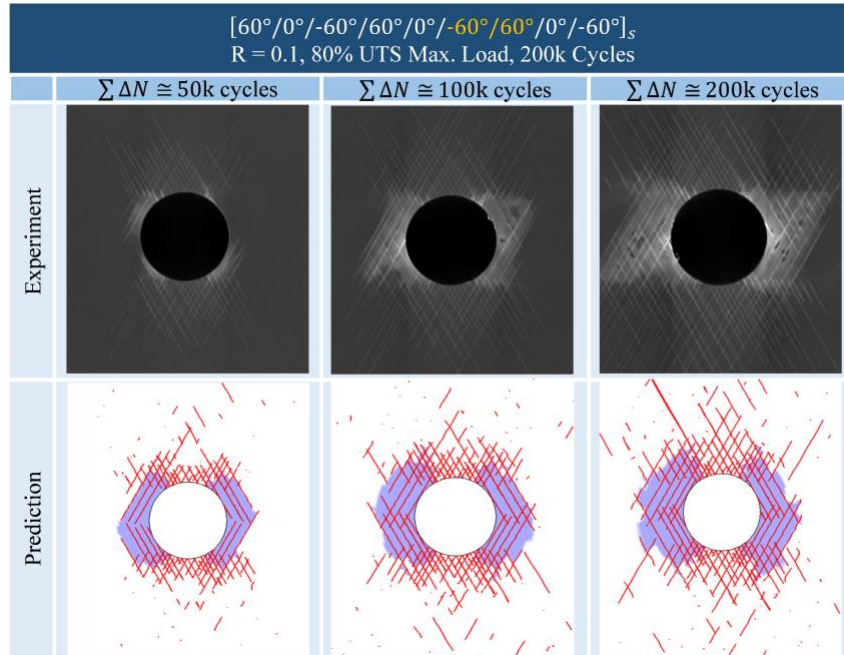
Figure 2.14 Damage evolution of inner -60 and 60 plies of the $[60°/0°/-60°]_{3s}$ layup after 50k, 100k, and 200k

cycles

In all images the thin grey lines in the experimental and red lines in the prediction

represent the matrix cracks, and the white and blue areas represent delamination in the

experimental and the BSAM results respectively. In the first image of Figure **2.12**, the crack path,

shown as black lines displays the RXFEM closed and open matrix cracks and is limited to the

user-defined domain boundary. The middle picture of Figure **2.12** shows open cracks in which the

damage variable is equal to one with two primary 30° and many short 60° cracks extending

outwards from the hole. Delamination is found extended outwards from the hole, constrained by

the matrix cracks. In the experimental inter 45°/90° interface of Figure **2.13** depicts short 90°

cracks extending outwards at a -45° because of the ply below. Close to the hole, longer 90°

cracks are found at the top and bottom of the hole along with 45° cracks with very little

delamination. The prediction follows closely to the mentioned damage. Lastly, Figure **2.14** shows

the damage propagation as the number of cycles accumulate. A high quantity of crossing 60° and

-60° cracks are observed starting around the hole and expanding to the outer edges of the specimen in both the prediction and experiment. Delamination is found expanding on the left and right side of the hole bounded by the crossing cracks. For further images from this case study, the reader is directed to Figure **6.1** through Figure **6.3** in the Appendix.

The above cases show the accurate crack depiction, propagation, and density of the RXFEM and CZM methodologies implemented in BSAM at the coupon level and will be used in the analysis of the current work.

3   Current Work

The model used throughout the open hole tests in the current work is obtained from the Advanced Material Characterization and Structural Certification, AMSC, report developed by the Air Force Research Laboratory, AFRL, and the National Institute for Aviation Research, NIAR and will involve higher cycle counts [62]. The current work will focus on verification of fatigue damage found in experimental tests using BSAM of three loading conditions tension-tension, compression-compression, and compression-tension found in the report. The purpose of the work is to ensure that fatigue damage at different loading types of laminate composites can accurately be predicted using an FEA software. The Current Work chapter will, in order, contain model specifications, a mesh study, and both static and fatigue analysis.

3.1   Model Specifications

3.1.1   Model Geometry, Material and Layup

The specimen used throughout the study is a rectangular coupon measuring 304.8 mm long, 38.1 mm wide, and 3.3 mm thick (12.0 in x 1.5 in x 0.1296 in). A 6.4 mm (0.252 in)

diameter hole is located at the center of the specimen. The model is created in Abaqus in which

only half the layup is modeled because of symmetry. A 38.1 mm by 44.45 mm loading tab is

added at the positive x-axis edge of the layup to carry the applied stress appropriately to the

specimen. The model geometry can be visualized in Figure **3.2** and Figure **3.3**.

The composite follows a $[45/0/-45/90]_{3s}$ layup made from IM7/5320-1, which the

properties can be viewed in Table 3. Comparing the material properties of IM7/5320-1 and

IM7/977-3 used in previous analysis, a much higher shear and compressive strength, both

longitudinal and transverse, is found. A decrease in both modes' critical ERR is observed.

Table 3 IM7/5320-1 Material Properties

Property	IM7/5320-1	Unit
E_{11}	157.2	GPa
E_{22}, E_{33}	9.38	GPa
G_{12}, G_{13}	5.03	GPa
G_{23}	3.24	GPa
v_{12}, v_{13}	0.30	
v_{23}	0.496	
α_1	0.00	
α_2	30.0 E -6	1/C
G_{IC}	0.226	N/mm
G_{IIC}	0.511	N/mm
Y_T	81.0	MPa
Y_C	312.0	MPa
S	133.8	MPa
X_T	2490	MPa
X_C	1990	MPa
S_1	0.026	
S_2	0.071	
m_1	11.38	
m_2	5.86	
C_1	0.039	mm
C_2	0.021	mm

Equations (2-67)-(2-71) provide the expression for S-N parameters as a function of R ratio. However, the independent measurement of the shear S-N relation for R=-1 performed for a similar material IM7/8552 does not follow this trend [63]. Figure **3.1** shows the trend line for the R = 0.1 and R = -1 functions of Equations (2-67)-(2-71) and the experimental results of IM7/8552 at R = -1. Due to significant difference between the measured and predicted trend line, it was decided to use an R= -1 relation which follows the experimental data by shifting the static shear strength to ~73% of the original static strength, therefor S_L=93.7 MPa was used in the compression-tension analysis. The initial S_2 was not changed during this procedure as the deduction rates across all loading conditions remained closely identical.
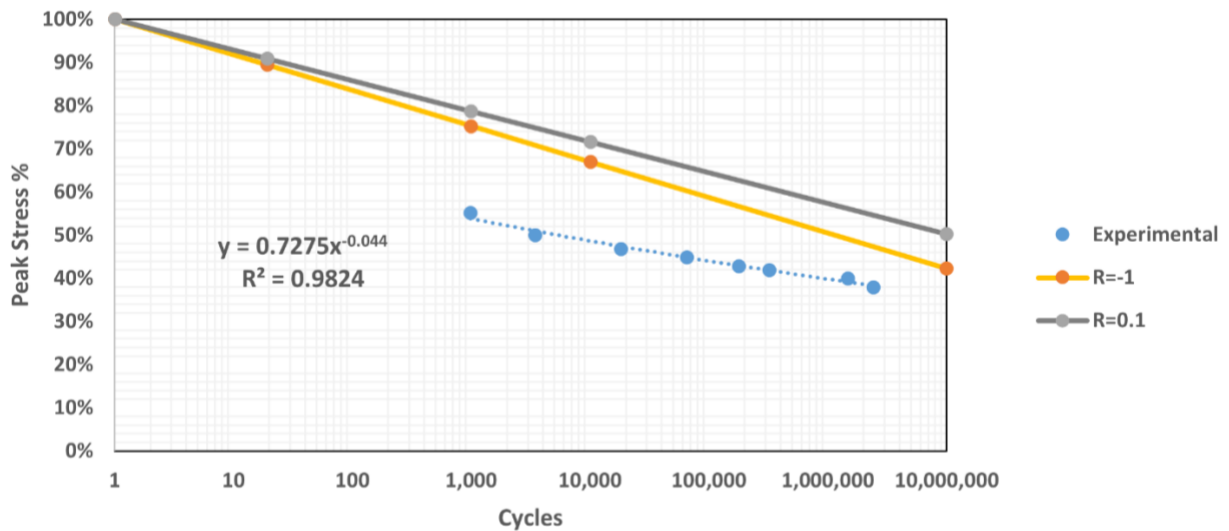
Figure 3.1 S-N curve used for compression-tension analysis
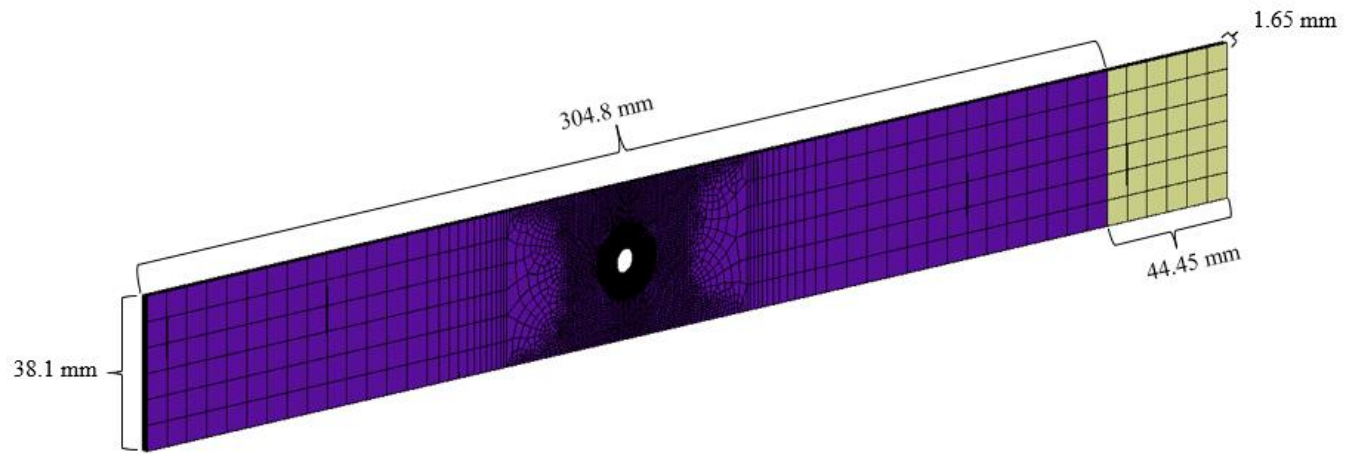
Figure 3.2 Model outer dimensions
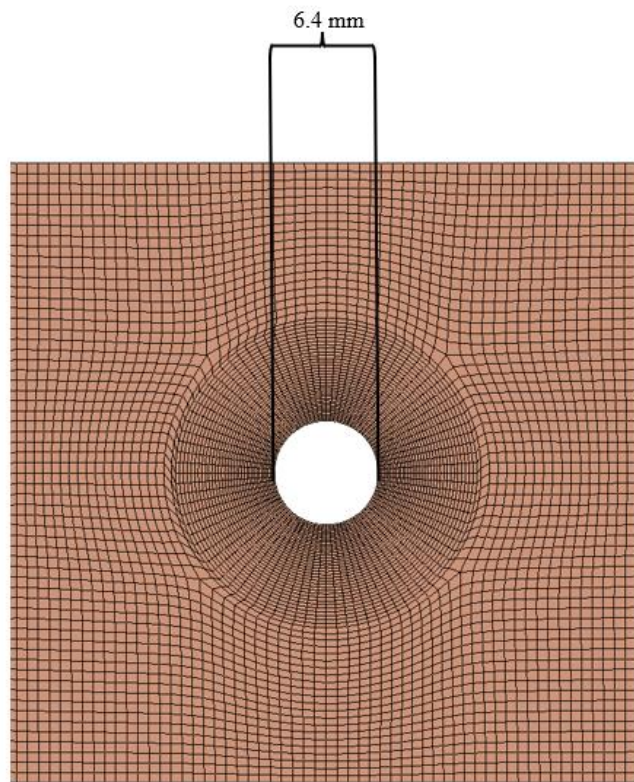
Figure 3.3 Model hole dimensions

45

3.1.2 Meshing and Boundary Conditions

Each ply consists of a single element through the thickness and six elements through the width at the outer regions of the specimen. The mesh begins to get finer towards the middle of the specimen, in which the finest is found around the area of interest, consisting of a size twice the diameter of the specimen's hole. Elements around the hole varied circumferentially from 0.250 mm to 0.625 mm and radially from 0.125 mm to 0.250 mm. The mesh size around the hole used throughout the analysis was determined by performing a parametric study to provide accurate results while also retaining computational efficiency and will be discussed in the next section. C3D8 elements were used aimed to be as square as possible in the area of interest to provide accurate damage propagation form the Paris Law.

The boundary conditions applied to the model to simulate the environment the specimen would endure during the physical experiment. An imposed $u_x = 0$ constraint is placed on the faces of all plies at the negative x-axis, simulating the non-loading grip found in the experiment. The midplane ply is constrained in the z-direction, $u_z = 0$, on the negative z-axis face to prevent unwanted displacements along the z-axis. Two nodes on both sides of the mid-plane ply are constrained in the y direction, $u_y = 0$ to prevent any twist in the model. To simulate the loading on the specimen, a uniform stress is applied on the positive x-axis face of the loading block. Lastly, a temperature change $\Delta T = -180$ is imposed to simulate the residual stresses from the curing process.

3.2 Mesh Study

Three different mesh sizes around the hole of the specimen were analyzed to determine an optimal size for balancing computational efficiency and accurate results as cycle counts found in

the experiment, specifically tension-tension, are much higher than what is normally performed with BSAM. Only the region of interest was considered as much of the damage across all tests are found around the hole.

In each study, the mesh sizing is changed both radially and circumferentially in the area of interest. The finer mesh consists of elements that are 0.2 mm through the circumference at the hole edge and 0.5 mm at the outer region of interest. The element size is radially increased outwards from the hole from 0.1 mm to 0.2 mm. A course mesh is then generated following the same guidelines as the fine mesh. The element size around the circle, circumferentially, is 0.4 mm and is 1.0 mm at the outer region of interest. The element size radially increases outward from 0.2 mm to 0.4 mm. Lastly, a mesh size in between was chosen with elements sizes from 0.25 mm to 0.625 mm circumferentially and 0.125 mm to 0.25 radially. All three meshes can be visualized in Figure **3.4**-Figure **3.6**.
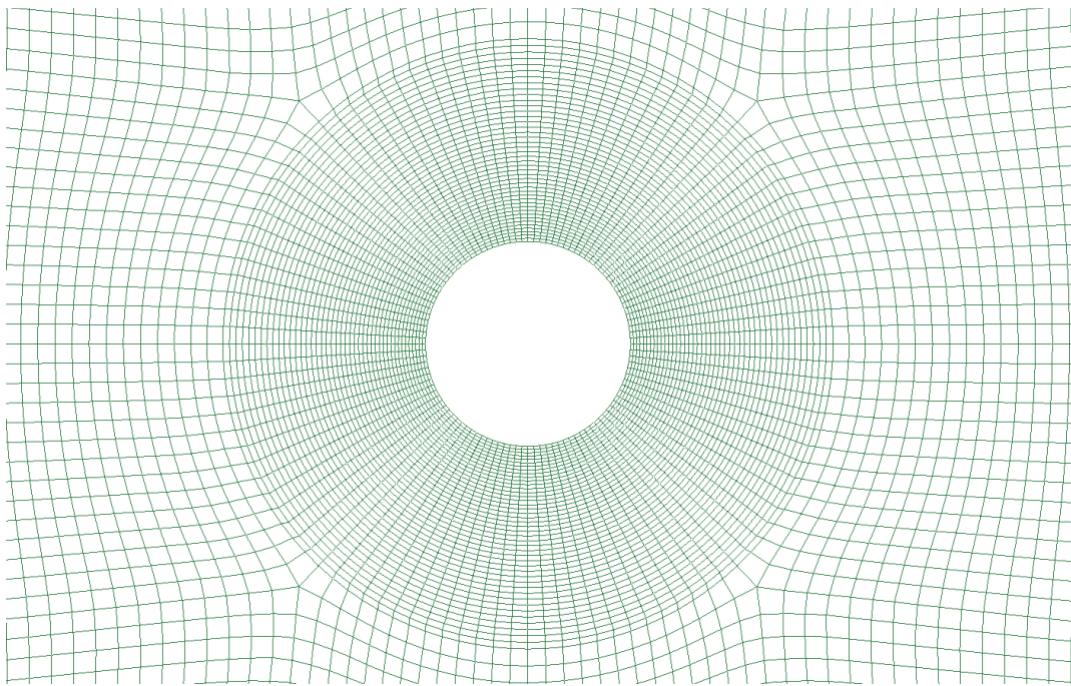
Figure 3.4 Fine mesh around specimen hole
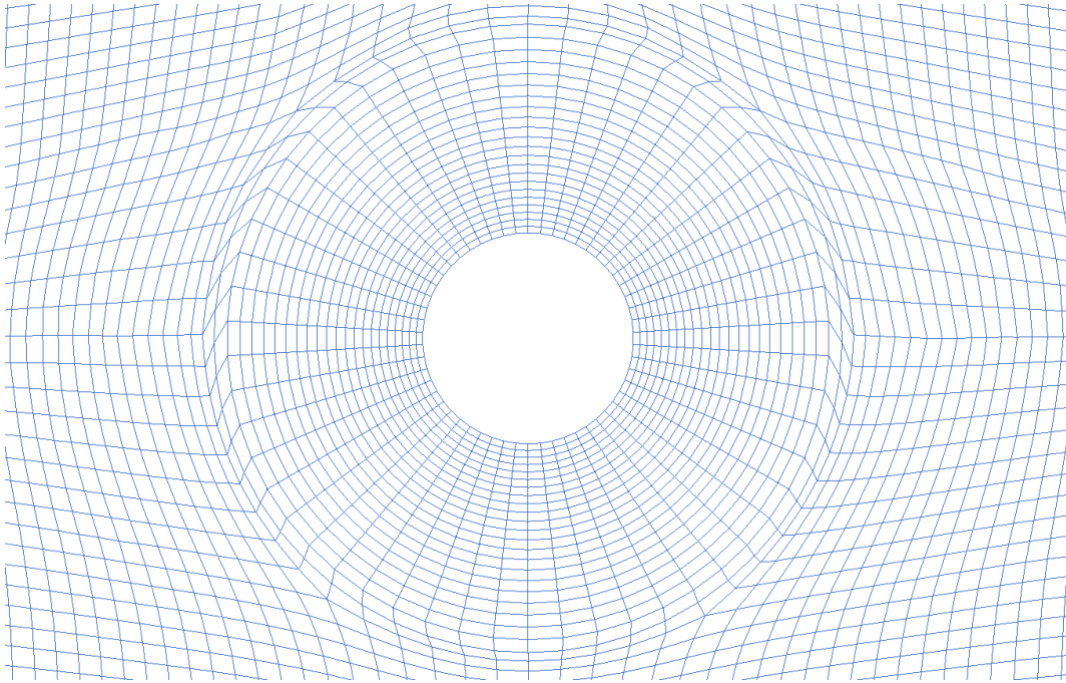
Figure 3.5 Coarse mesh around specimen hole
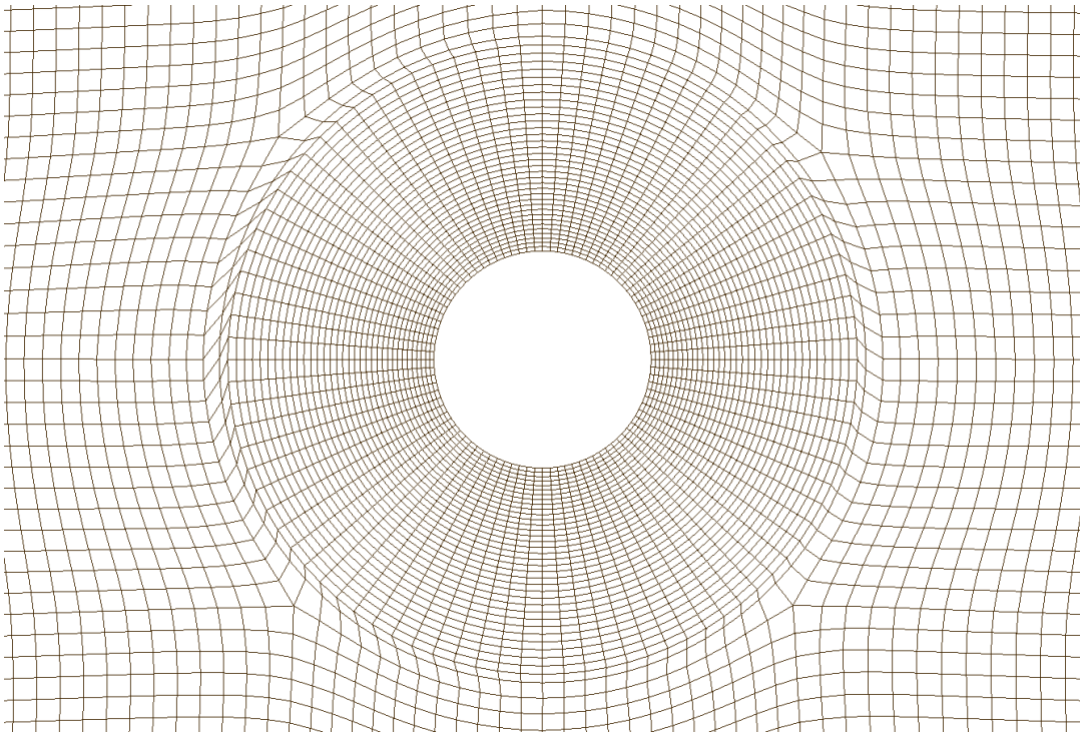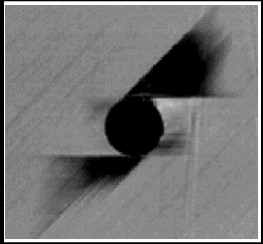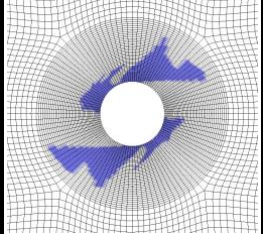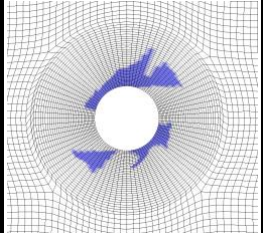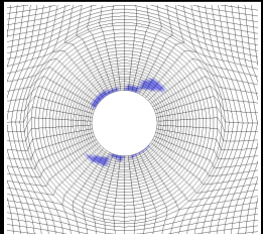
Figure 3.6 Medium mesh around specimen hole

All three meshes were used in an OHT-T fatigue test with an applied load of 80% of the static strength of IM7/5320-1 to analyze the impact of the mesh sizing on results and analysis time. Since the highest loading for of the NIAR experiments reach a run-out of one million cycles for the OHT-T tests, it was a goal for each mesh to reach this point at the end of the FEA analysis. A table comprising of the final cycles reached and the time for the mesh to reach that point can be found in Table 4.

Table 4 Mesh analysis final cycle and run time

Mesh Sizing	Final Cycle	Analysis Run Time
Fine	383,340	15d 0h (Max)
Medium	1,000,000	5d 0h
Coarse	1,000,000	1d 8h

Without looking at the damage results, the fine mesh was not able to reach the desired million cycles and took the maximum run time allowed by the high-performance computing. This is highly undesirable in validating damage with experimental work if the analysis is unable to reach the cycles performed in the experiment. Computational efficiency is also of high priority in validating results in a timely manner and having too fine of a mesh greatly increases the computational time. The medium and coarse mesh were able to reach the million cycles in substantially less time than the fine mesh, making both possible choices in terms of computationally efficiency.

	Result
Experimental	
Fine Mesh	
Medium Mesh	
Coarse Mesh	

Figure 3.7 Delamination in different meshes compared with experimental result

Comparing the different meshes one can observe differences as the mesh is getting coarser. The fine mesh provides the most accurate result than the others. The medium mesh follows the same damage pattern as the experimental but to a smaller extent. The coarse mesh is seen show very little damage and does not accurately depict the experimental damage.

Considering analysis time and the ability to accurately depict damage accumulation, the medium mesh was chosen for the current work.

3.3 Static Analysis

The first step in the current work was to reproduce static strength data obtained in the experimental procedures. The goal of the static FEA was to be within a five percent threshold for both compression and tension tests. In the static analysis, instead of a loading block used in the fatigue, a uniform displacement was applied on the positive x-faces of each ply in the layup. After the static simulation is complete, the force-displacement data or Critical Volume Failure (CFV) of the zero-degree plies is obtained through post-processing to determine static failure.

3.3.1 Tension

CFV was used in the tension-tension static analysis to determine static strength of the specimen. Using load factor data produced by the analysis, the obtained stress before single ply failure of one of the zero-degree plies was determined to be 433 MPa. Comparing this value with the experiment of 472 MPa, an 8.3% reduction in static strength is obtained. Although the percent error is outside the desired five percent, it is taken as a respectable value because of several factors found in the experimental tests and the result of mesh dependency.

3.3.2 Compression

For compression verification, force-displacement data from the simulation was used, taking the stress just before a load drop-off as the static strength. An iteration process was performed reducing the fiber compression fracture toughness to reach the five percent threshold as fiber failure is the reason for specimen failure. Through this process, the fiber compression fracture toughness was reduced from 20.0 to 8.0 N/mm and the resulting static strength from the compression analysis was obtained to be -361 MPa. Comparing with the static strength found in the physical experiment, -350 MPa, the FEA had a 3.1% difference in static strength. The static

strength value in compression was used in both the compression-compression and compression-tension analysis, just as it was used in the experimental work. In the traction-displacement curve of Figure **3.8** the initial displacement is non-zero because of thermal effects applied before compression.
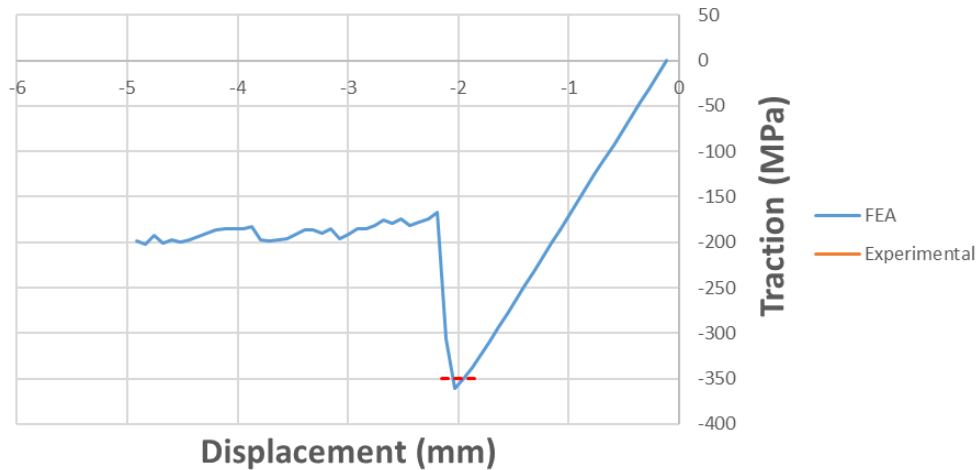
Figure 3.8 Traction-displacement curve for compression static test

3.4 Fatigue Analysis

3.4.1 Tension-Tension

The analysis of the tension-tension specimen is centered on delamination size and shape rather than fiber failure that is observed in the compression-compression results. For the tested specimen, fatigue analysis was performed to the experimental runout of one million cycles with an applied load of 90% the ultimate stress. From the experimental images found in the AMCSC report the interfaces at the top and bottom of the specimen between the outer 45°/0°, 0°/-45°, and -45°/90° were compared with the results found in the simulation result. The inner plies of the

52

experimental specimen were not chosen for comparison because of lack of damage observed in the provided images.
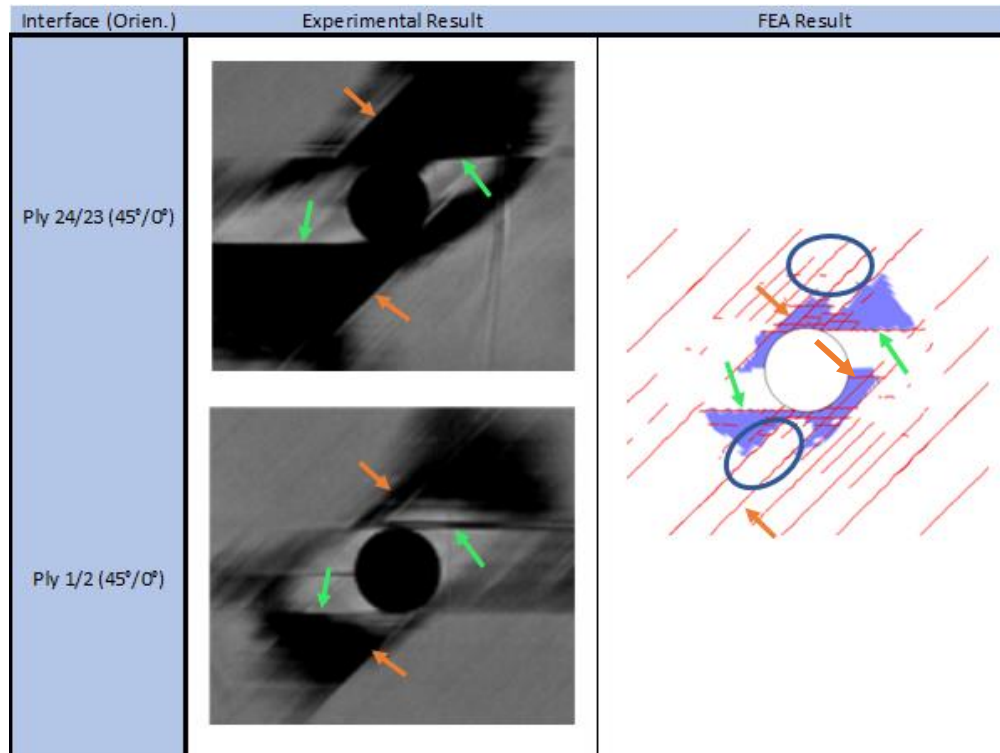
Figure 3.9 OHT-T interface-level damage comparison of 45°/0° interfaces

In the outermost interfaces of the layup, the greatest amount delamination can be observed, both in the experimental and the FEA result. In both experimental images, delamination is found on the top and bottom of the hole bounded by a 45-degree matrix cracks highlighted in orange and 0-degree cracks highlighted in green. The same matrix cracks, depicted in red, that bound delamination, depicted in blue, were found in the computation, creating the same delamination shape. However, the delamination size found in the FEA result was found to be smaller than what was found in the experimental results. In the computational result, two main 45-degree cracks limit the delamination expansion to only along the highlighted cracks where delamination originated, the additional long 45-degree cracks create regions where

53

delamination should be observed in the dark-blue highlighted areas. Another key area for delamination is found at the bottom right of the hole of the experimental images, expanding upwards connecting to the upper delamination damage region. This area is found in the FEA result; however, it does not extend completely to the upper delamination.
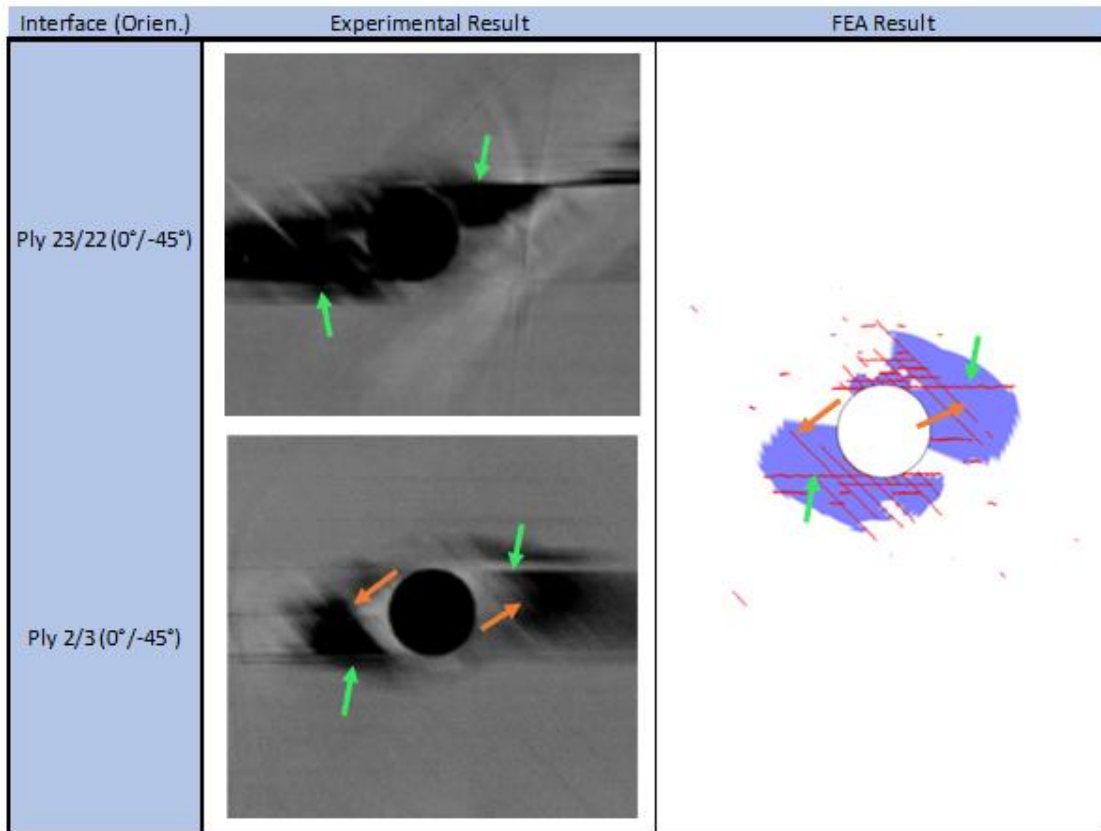
Figure 3.10 OHT-T interface-level damage comparison of 0°/-45° interfaces

The second set of interfaces discussed will be the 0°/-45° interfaces. In contrast to the previous interfaces, delamination was overpredicted in the computational analysis, expanding outside the diameter of the whole at the top and bottom. A much higher crack density of negative 45-degree cracks is found at the top and bottom of the hole which leads to the delamination in the FEA result that is not found in the experimental images. The 0-degree crack bound, emphasized by a green arrow, found in the experiment is also found in the FEA result. In the interface between ply 2 and 3, negative 45-degree cracks are noted in orange that bind the

delamination which are also found in the computational result. However, it is expected that because of poor image quality found in the experimental images, the delamination in the interface between ply 2 and 3 extends from the noted cracks to the hole of the specimen.
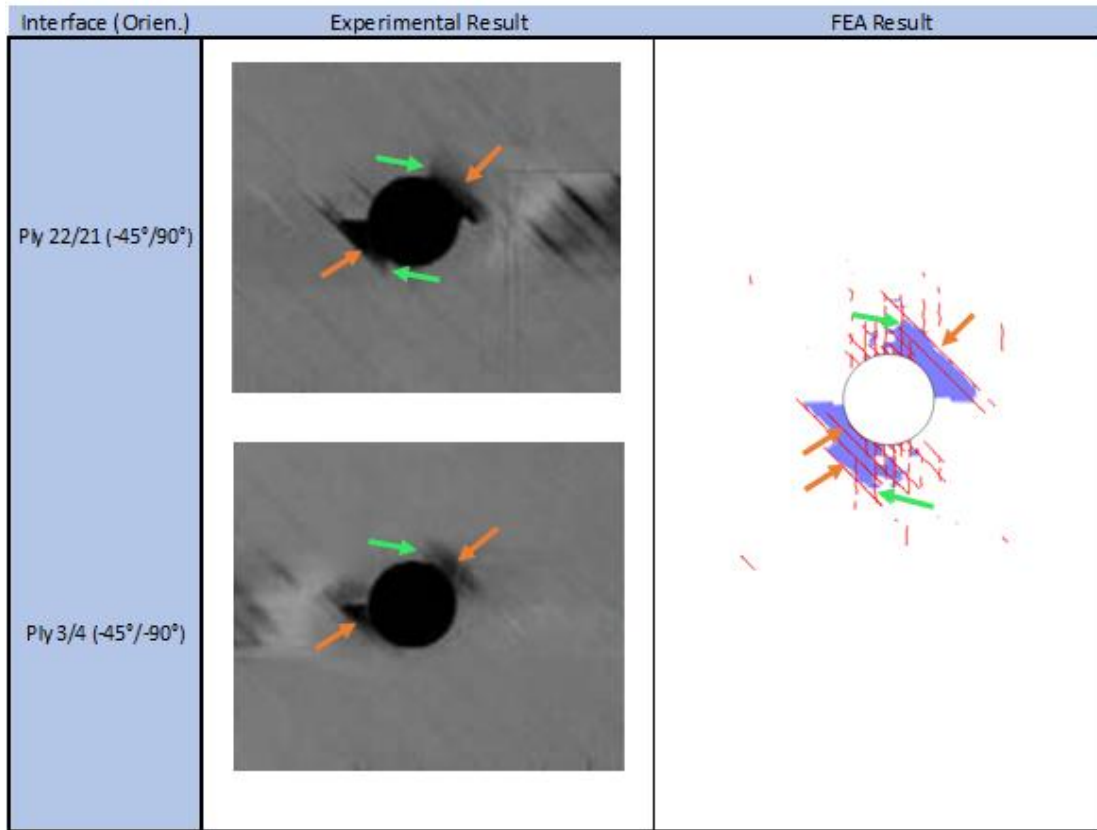
Figure 3.11 OHT-T interface-level damage comparison of -45°/-90° interfaces

The last interfaces that will be discussed in the OHT-T specimen will be the -45°/-90° interfaces. Out of the three, this was determined to be the most accurate in depicting delamination damage size and shape. In the experimental images, negative 45-degree cracks bound the delamination at the bottom-left and top-right of the hole, shown in orange. At the bottom-left of the hole, the interface of ply 22 and 21 is bounded by a negative 45-degree crack further from the hole than the crack found in the interface of ply 3 and 4, both cracks are found in the simulation. In the FEA result, a much higher crack density of 90-degree cracks is found on

55

the top and bottom of the hole, however, the experimental result only shows a few 90-degree

cracks highlighted in green.

3.4.2   Compression-Compression

For the fatigue analysis, the highest loading condition for compression-compression tests

was chosen of 80% of the static strength. Therefore, a uniform stress of -280 MPa was applied to

the loading tab at the end of the specimen. Failure during the mechanical testing found in the

report was determined to be at 8,673 cycles. Due to BSAM using cycle jump methodology, the

closest cycle step, 8,635, was used to compare damage. Two plies were used for validating fiber

damage in the specimen, ply 6 and ply 24 of the AMCSC report. Due to the images in the report

taken at the ply level and not the interface, delamination size and shape were unable to be

verified, instead normalized residual stiffness was captured using the force-displacement data

throughout the analysis and compared with the experimental results in Figure **3.12**. The FEA

analysis follows closely to the experiment residual stiffness curve up to just before failure, in

which a steep drop from the experiment data is observed.
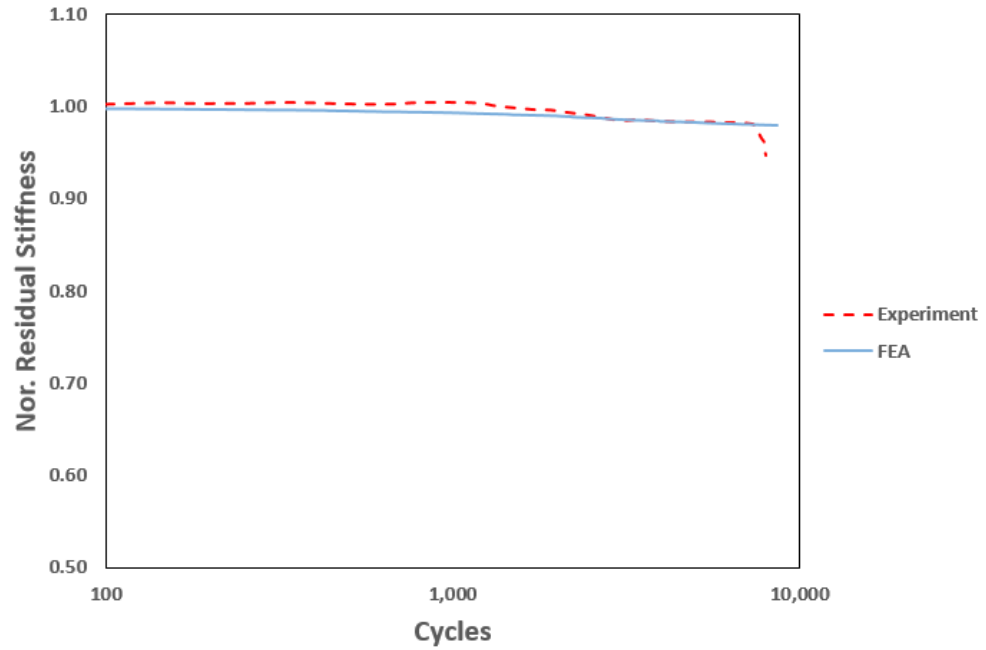
Figure 3.12 Normalized residual stiffness curve
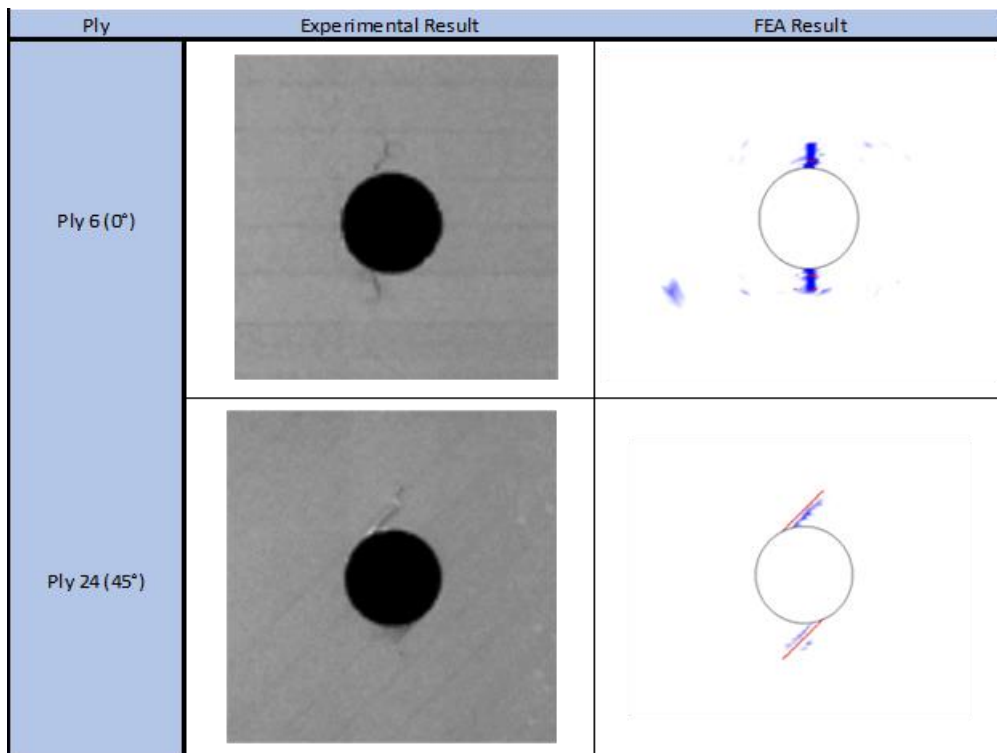
Figure 3.13 OHC-C ply-level damage comparison

The visual damage comparison between the experimental and FEA results can be found in Figure **3.13**. In the OHC-C result, blue regions are CDM damage representing fiber failure.
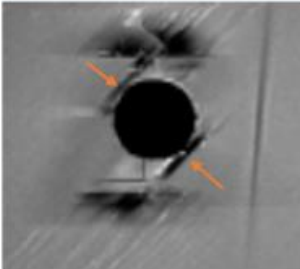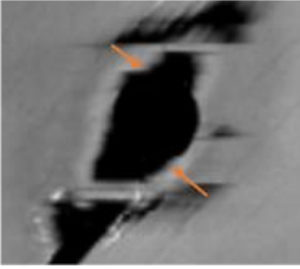
First observing the inner zero-degree ply, ply 6, fiber failure is seen at the top and bottom of the hole expanding in the ninety-degree direction, for both experiment and FEA results. The result obtained from the FEA analysis shows proper fiber damage size. One difference found between the experiment and FEA result is the fiber damage location, in the experimental result the damage is found to be off-center of the circle compared to the fiber failure centered on the hole in the FEA result.

In ply 24, the outermost forty-five-degree ply, fiber damage can be seen in the experiment result expanding from the top-left and bottom-right along the fiber direction. This same result can be observed in the FEA result. At the top of the hole, the fiber damage is guided by a matrix crack which can also be observed in the experimental result. Fiber damage in the analytical result is seen to be both the appropriate size and location.

3.4.3   Compression-Tension
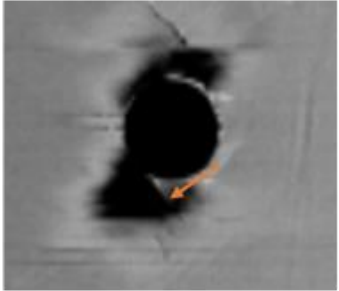
The last analysis performed in the current work was compression-tension. The compression-tension analysis uses the static results found in the compression tests, as what is performed in the NIAR experiments. The highest loading conditions were chosen for the analysis, therefor 60% of the compression strength is applied as a uniform stress on the loading tab, -210 MPa. Failure in the experiment occurred at 37,365 cycles and the analytic step corresponding to 37,463 was examined. Several plies will be compared with the experimental images, showing the different damage types found in compression-compression and tension-

58

tension specimens all in the compression-tension analysis. The first set of interfaces that will be examined are the outer 45/0-degree interfaces in Figure **3.14**.
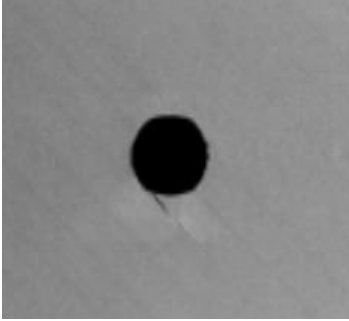

Figure 3.14 OHC-T interface-level damage comparison of 45°/0° interfaces

The delamination found in the outer 45/0-degree interfaces are bound by 45-degree cracks extending from the bottom right and top left of the hole, which is predicted in the FEA analysis and are shown in orange. The computation predicts 0-degree cracks originating at the bottom and top of the hole but are unable to be seen in the experimental results because of the delamination. The delamination around the hole in the interface between plies 1 and 2 resemble closely in size and shape of that found in the FEA result.

Interface (Orien.)	Experimental Result	FEA Result
Ply 23/22 (0°/-45°)		

Figure 3.15 OHC-T interface-level damage comparison of 0°/-45° interfaces

Only one of the 0/-45-degree interfaces were able to be compared, in Figure **3.15** because of quality of the experiment image found in the other interface. The highlight of this interface and the simulated result is the -45-degree crack extending at the bottom-left of the hole. In the experimental result delamination is mostly constricted from expanding to the right side of this crack, however, the simulation shows delamination in this region. Other cracks that are found in the FEA result are unable to be verified in the experiment's image because of the delamination observed. Delamination found at the top of the hole matches significantly with the experimental result but delamination size at the bottom of the hole is slightly smaller and a slightly different shape.

The interfaces between -45/90-degree plies were found to have little damage, both in the FEA result and experiment. However, compared with the previous interfaces, cracks from both plies can be seen. The crack lengths found in the FEA result were determined to be shorter than those found in the experimental result, but the location and effect on delamination is observed to be the same. Two -45-degree cracks are found at the top and bottom of the hole, pointed to in orange, while two 90-degree cracks, pointed to in green, are found almost centered at the top and
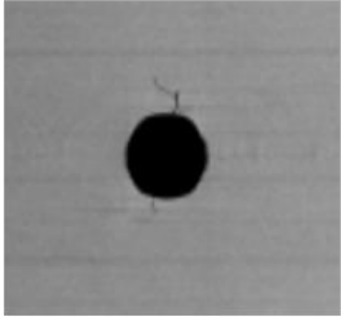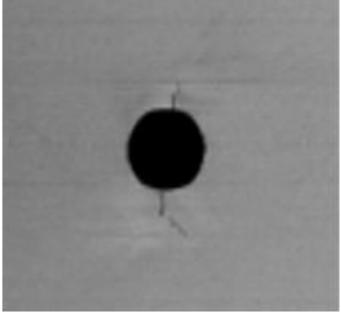
bottom of the hole. Delamination size is very small and most noticeably found in the interface between plies 22 and 21, which is predicted in the FEA result.
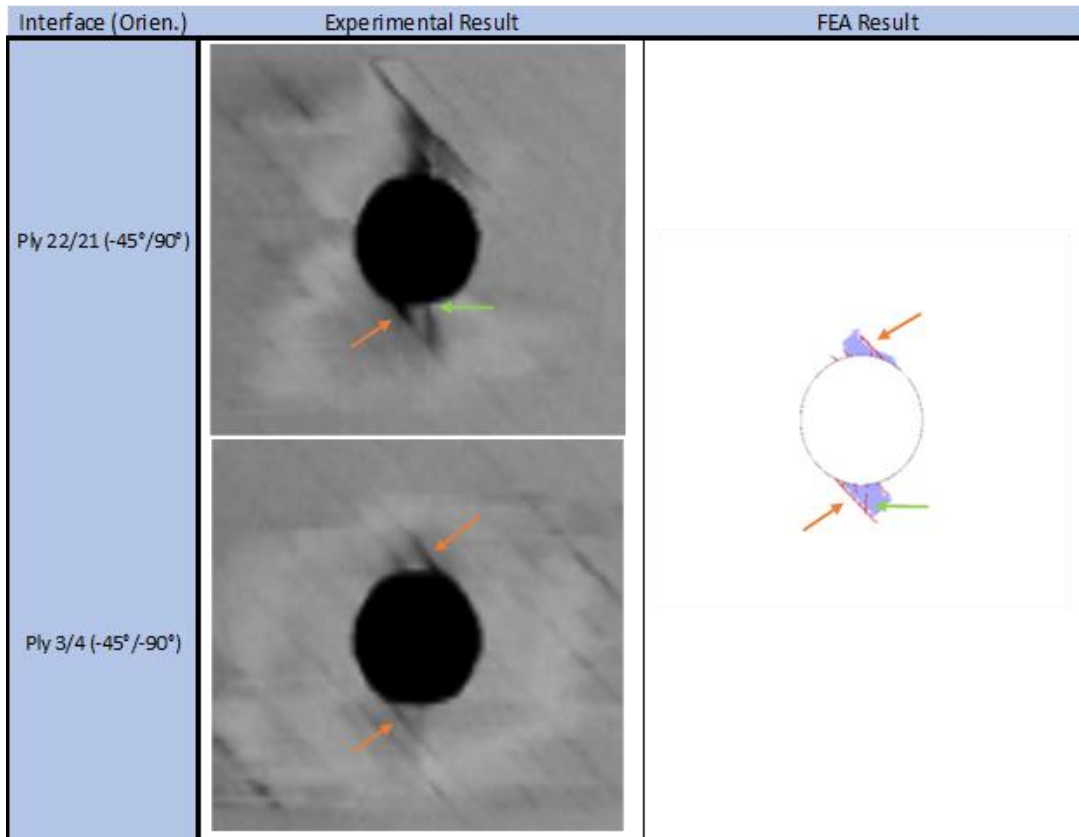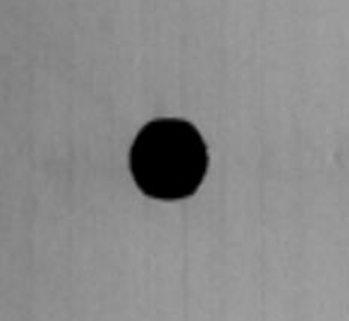
Figure 3.16 OHC-T interface-level damage comparison of -45°/90° interfaces

Fiber failure was only found in the 0-degree plies, much like the compression-compression analysis previously. The experimental images are taken at the ply level and delamination will not be able to be observed and no matrix cracks are seen. The fiber failure is predicted at the top and bottom of the hole at the center, shown in blue in the FEA result much like the compression-compression results. The length of the fiber damage is much shorter than the experimental results.

Figure 3.17 OHC-T ply-level damage comparison of 0° plies

The last set of interfaces that will be discussed are two inner interfaces, shown in Figure **3.18**, where minimal damage is found including no delamination. Only short matrix cracks can be viewed in the FEA analysis, correlating well with the experimental results.

Interface (Orien.)	Experimental Result	FEA Result
Ply 14/13 (-45°/90°)		
Ply 17/16 (90°/45°)		

Figure 3.18 OHC-T interface-level damage comparison of inner interfaces

3.5 Paris Law Parametric Study

Throughout the OHT-T analysis an increase in delamination and matrix crack size was desired to reach closer results to the experimental images. As delamination growth and crack propagation is governed by the Paris Law, coefficients of mode I were raised based off NIAR's experimental results showing greater variance from the average trend line of testing the specimen in a DCB model setup. Mode II propagation data followed closely to the average trend line and the coefficients were left unchanged.
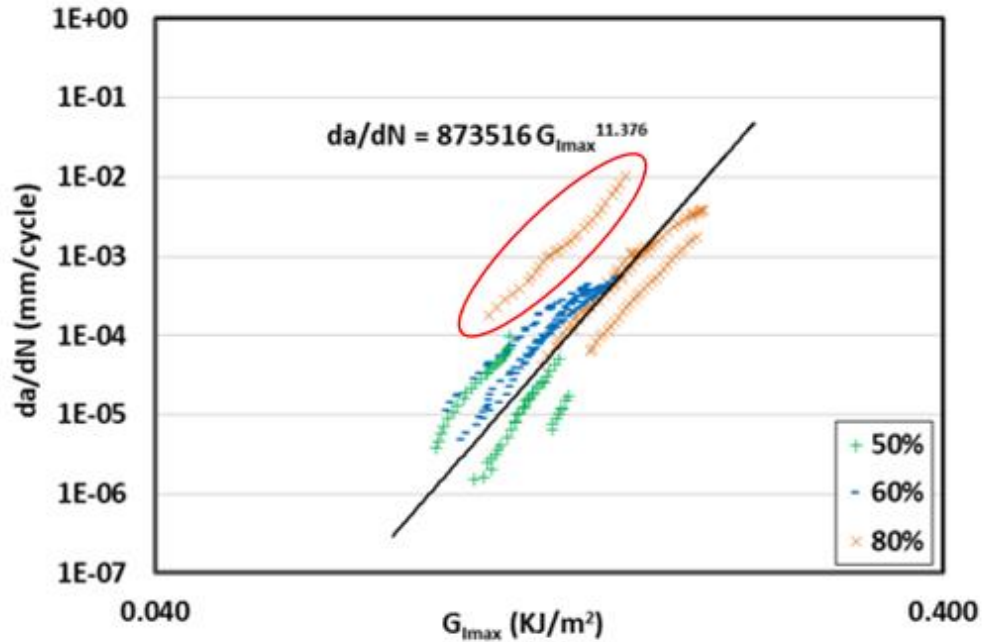
Figure 3.19 Mode I crack growth from experimental results of IM7/5320-1

The solid black line found in Figure **3.19** was found to be the best fit line for propagation rates for all three loading aptitudes and was chosen as the basis for mode I coefficients in the analysis for the current work. However, to increase the crack growth the upper bound propagation rate, highlighted in red, in the experimental results was extracted. Comparison of the coefficients can be found in the following table.

Table 5 Mode I coefficient comparison

	C_1	M_1
Original	0.039	11.38
Updated	0.285	9.79
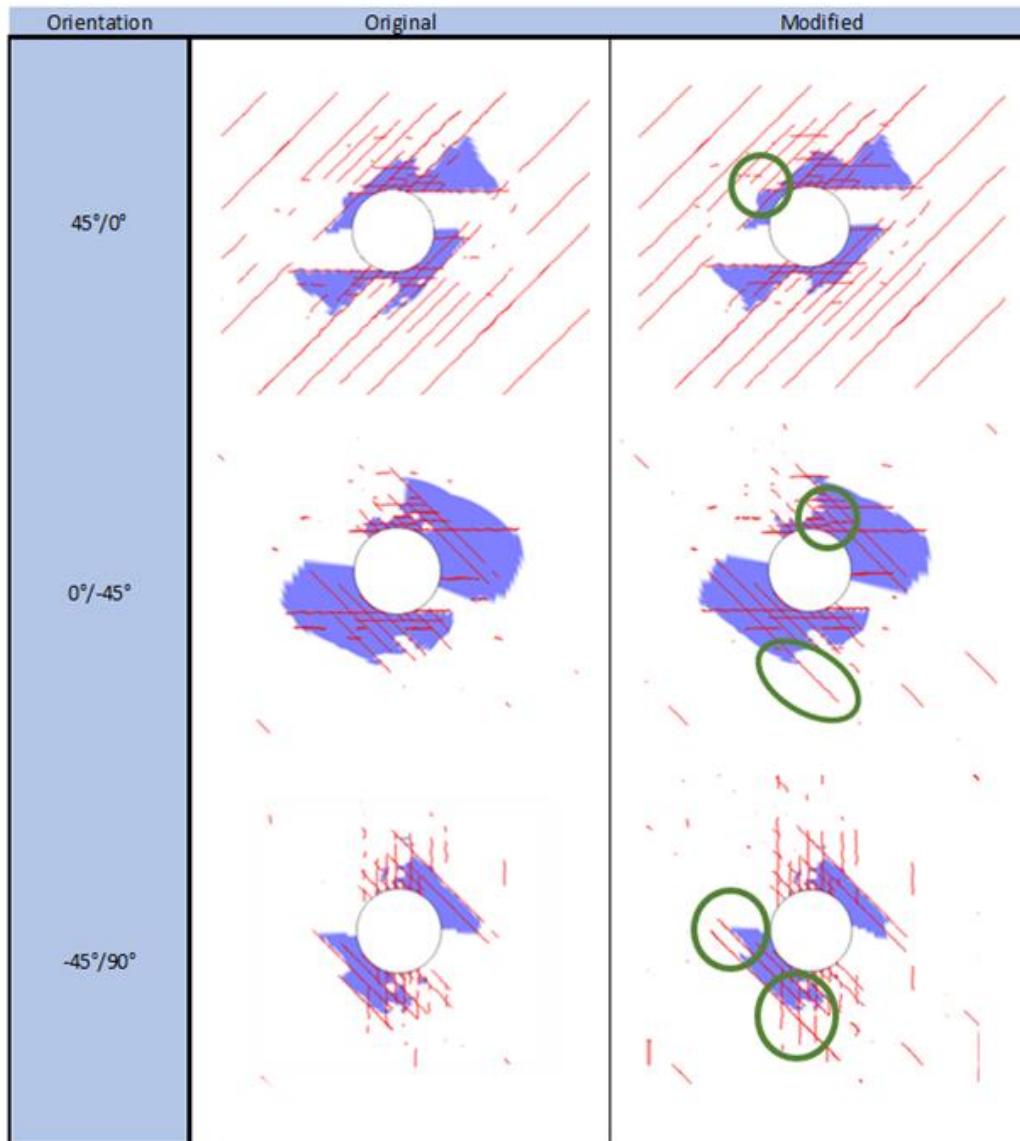
Figure 3.20 Paris Law parametric study results

Comparing the results of changing the mode I Paris Law coefficients found in Figure **3.20**, no drastic changes can be observed between the original and modified results. The only differences found in the modified results are emphasized in green, which mostly are larger matrix crack lengths. The modified Paris Law had minimal impact on delamination size and from this parametric study it was determined that modifying mode I coefficients would have minimal effect on analytic results.

4 Conclusions

Static and fatigue analysis was performed using the FEA software BSAM on advanced out-of-autoclave composites to compare delamination, matrix cracking, and fiber failure accumulation with experimental data. RXFEM methodology was used for modeling damage. CZM and strength tracking methodologies were used for crack propagation throughout the fatigue analysis. The Local-R ratio was monitored throughout the analysis to obtain accurate load ratios and for algorithm updating. Fiber failure was modeled using CDM techniques. Three cases, tension-tension, compression-compression, and compression-tension were examined for an open-hole IM7/5320-1 quasi-isotropic laminate.

The damage accumulation in each case was compared with the experimental results studied by NIAR in the Advanced Material Characterization and Structural Certification report. From this study, key similarities and some differences are found with the experimental specimens and the computational analysis. The tension-tension results showed overall results close to experimental data for delamination and matrix cracking of outer ply interfaces. Fiber failure was the only damage mode clearly identifiable in experiment in the compression-compression case. It was also predicted in the 0-degree and 45-degree plies in the same location and size as observed in the experiment. Lastly, the compression-tension analysis contained all three damage modes. Delamination shape was consistent in both cases but smaller in size than in the FEA. Similarly, the fiber failure mode was found in 0-degree plies but to also smaller extent than in the experiment.

5 References

[1]   Quilter, A. "Composites in Aerospace Applications." *IHS White Paper*, Vol. 444, No. 1,2001, p. 264.

[2]   Rana, S., and Fangueiro, R. Advanced Composites in Aerospace Engineering. In *Advanced Composite Materials for Aerospace Engineering*, Elsevier, 2016, pp. 1–15.

[3]   United States Government Accountability Office. *Aviation Safety: Status of FAA's Actions to Oversee the Safety of Composite Airplanes*. 2011.

[4]   Talreja, R., and Singh, C. V. *Damage and Failure of Composite Materials*. Cambridge University Press, 2012.

[5]   Maimí, P., Camanho, P. P., Mayugo, J. A., and Dávila, C. G. "A Continuum Damage Model for Composite Laminates: Part I - Constitutive Model." *Mechanics of Materials*, Vol. 39, No. 10, 2007, pp. 897–908. https://doi.org/10.1016/j.mechmat.2007.03.005.

[6]   Abrate, S. "Matrix Cracking in Laminated Composites: A Review." *Composites Engineering*, Vol. 1, No. 6, 1991, pp. 337–353. https://doi.org/10.1016/0961-9526(91)90039-U.

[7]   Jamison, R. D. "The Role of Microdamage in Tensile Failure of Graphite/Epoxy Laminates." *Composites Science and Technology*, Vol. 24, No. 2, 1985, pp. 83–99. https://doi.org/10.1016/0266-3538(85)90053-3.

[8]   Novak, J. *A Comparison of Discrete Damage Modeling Methods: The Effect of Stacking Sequence on Progressive Failure of the Skin Laminate in a Composite Pi-Joint Subject to Pull-off Load*. The University of Texas at Arlington, 2019.

[9]   Sridharan, S. *Delamination Behaviour of Composites*. Elsevier, 2008.

[10]   ARGON, A. S. Fracture of Composites. 1972, pp. 79–114.

[11]   Bishara, M., Rolfes, R., and Allix, O. "Revealing Complex Aspects of Compressive Failure of Polymer Composites – Part I: Fiber Kinking at Microscale." *Composite Structures*, Vol. 169, 2017, pp. 105–115. https://doi.org/10.1016/j.compstruct.2016.10.092.

[12]   Hossain, M. S. *FINITE ELEMENT BASED METHODOLOGY TO PREDICT FATIGUE COMPRESSION FAILURE IN COMPOSITE BASED ON FIBER KINKING DAMAGE MODEL*. University of Texas at Arlington, Arlington, 2020.

[13]   Steif, P. S. "A Model for Kinking in Fiber Composites—II. Kink Band Formation." *International Journal of Solids and Structures*, Vol. 26, Nos. 5–6, 1990, pp. 563–569. https://doi.org/10.1016/0020-7683(90)90029-U.

[14]   Krajcinovic, D., and Lemaitre, J. *Continuum Damage Mechanics Theory and Application*. Springer Vienna, 1987.

[15]   Kachanov, L. "Time of the Rupture Process under Creep Conditions." *Izvestiia Akademii Nauk SSSR*, 1958.

[16]   Maimí, P., Camanho, P. P., Mayugo, J. A., and Dávila, C. G. "A Continuum Damage Model for Composite Laminates: Part II – Computational Implementation and

Validation." *Mechanics of Materials*, Vol. 39, No. 10, 2007, pp. 909–919. https://doi.org/10.1016/j.mechmat.2007.03.006.

[17]   Llobet, J., Maimí, P., Essa, Y., and Martin de la Escalera, F. "A Continuum Damage Model for Composite Laminates: Part III - Fatigue." *Mechanics of Materials*, Vol. 153, 2021, p. 103659. https://doi.org/10.1016/j.mechmat.2020.103659.

[18]   Camacho, G. T., and Ortiz, M. "Computational Modelling of Impact Damage in Brittle Materials." *International Journal of Solids and Structures*, Vol. 33, Nos. 20–22, 1996, pp. 2899–2938. https://doi.org/10.1016/0020-7683(95)00255-3.

[19]   Iarve, E. V., Hoos, K. H., and Mollenhauer, D. H. Damage Initiation and Propagation Modeling in Laminated Composites under Fatigue Loading. 2016.

[20]   Greco, F., Leonetti, L., Lonetti, P., and Nevone Blasi, P. "Crack Propagation Analysis in Composite Materials by Using Moving Mesh and Multiscale Techniques." *Computers & Structures*, Vol. 153, 2015, pp. 201–216. https://doi.org/10.1016/j.compstruc.2015.03.002.

[21]   Branco, R., Antunes, F. V., and Costa, J. D. "A Review on 3D-FE Adaptive Remeshing Techniques for Crack Growth Modelling." *Engineering Fracture Mechanics*, Vol. 141, 2015, pp. 170–195. https://doi.org/10.1016/j.engfracmech.2015.05.023.

[22]   Fabbrocino, F., Funari, M. F., Greco, F., Lonetti, P., Luciano, R., and Penna, R. "Dynamic Crack Growth Based on Moving Mesh Method." *Composites Part B: Engineering*, Vol. 174, 2019, p. 107053. https://doi.org/10.1016/j.compositesb.2019.107053.

[23]   Moës, N., Dolbow, J., and Belytschko, T. "A Finite Element Method for Crack Growth without Remeshing." *International Journal for Numerical Methods in Engineering*, 1999.

https://doi.org/10.1002/(SICI)1097-0207(19990910)46:1<131::AID-NME726>3.0.CO;2-J.

[24] Swindeman, M. J., Iarve, E. V., Brockman, R. A., Mollenhauer, D. H., and Hallett, S. R. "Strength Prediction in Open Hole Composite Laminates by Using Discrete Damage Modeling." *AIAA Journal*, Vol. 51, No. 4, 2013, pp. 936–945. https://doi.org/10.2514/1.J051773.

[25] Singh, I. V., Mishra, B. K., Bhattacharya, S., and Patil, R. U. "The Numerical Simulation of Fatigue Crack Growth Using Extended Finite Element Method." *International Journal of Fatigue*, Vol. 36, No. 1, 2012, pp. 109–119. https://doi.org/10.1016/j.ijfatigue.2011.08.010.

[26] Mohammadi, S. *XFEM Fracture Analysis of Composites*. Wiley, 2012.

[27] Iarve, E. V. "Mesh Independent Modelling of Cracks by Using Higher Order Shape Functions." *International Journal for Numerical Methods in Engineering*, Vol. 56, 2003, pp. 869–882. https://doi.org/10.1002/nme.596.

[28] Cook, R. D., Malkus, D. S., Plesha, M. E., and Witt, R. J. *Concepts and Applications of Finite Element Analysis*. Wiley, 2001.

[29] Duarte, A. P. C., Díaz Sáez, A., and Silvestre, N. "Comparative Study between XFEM and Hashin Damage Criterion Applied to Failure of Composites." *Thin-Walled Structures*, Vol. 115, 2017, pp. 277–288. https://doi.org/10.1016/j.tws.2017.02.020.

[30] Pandey, V. B., Singh, I. V., Mishra, B. K., Ahmad, S., Venugopal Rao, A., and Kumar, V. "A New Framework Based on Continuum Damage Mechanics and XFEM for High Cycle

Fatigue Crack Growth Simulations." *Engineering Fracture Mechanics*, Vol. 206, 2019, pp. 172–200. https://doi.org/10.1016/j.engfracmech.2018.11.021.

[31]   Rege, K., and Lemu, H. G. "A Review of Fatigue Crack Propagation Modelling Techniques Using FEM and XFEM." *IOP Conference Series: Materials Science and Engineering*, Vol. 276, 2017, p. 012027. https://doi.org/10.1088/1757-899X/276/1/012027.

[32]   Swinderman, M. *A Regularized Extended Finite Element Method for Modeling the Coupled Crack and Delamination of Composite Materials*. Dissertation. University of Dayton, 2011.

[33]   Benvenuti, E., Tralli, A., and Ventura, G. "A Regularized XFEM Model for the Transition from Continuous to Discontinuous Displacements." *International Journal for Numerical Methods in Engineering*, Vol. 74, No. 6, 2008, pp. 911–944. https://doi.org/10.1002/nme.2196.

[34]   Iarve, E. V., Gurvich, M. R., Mollenhauer, D. H., Rose, C. A., and Dávila, C. G. "Mesh-Independent Matrix Cracking and Delamination Modeling in Laminated Composites." *International Journal for Numerical Methods in Engineering*, Vol. 88, No. 8, 2011, pp. 749–773. https://doi.org/10.1002/nme.3195.

[35]   Lu, W.-T., Gao, Z., Adluru, H. K., Hoos, K. H., Seneviratne, W. P., Mollenhauer, D. H., and Iarve, E. V. "Fatigue Damage Modeling in Laminated Composite by Using Rx-FEM and Strength Tracking Method." *Composites Part A: Applied Science and Manufacturing*, Vol. 163, 2022, p. 107199. https://doi.org/10.1016/j.compositesa.2022.107199.

[36]   Barenblatt, G. I. The Mathematical Theory of Equilibrium Cracks in Brittle Fracture. 1962, pp. 55–129.

[37]   Turon, A. *Simulation of Delamination in Composites under Quasi-Static and Fatigue Loading Using Cohesive Zone Models*. Thesis. Universitat de Girona, 2006.

[38]   Turon, A., Costa, J., Camanho, P. P., and Dávila, C. G. "Simulation of Delamination in Composites under High-Cycle Fatigue." *Composites Part A: Applied Science and Manufacturing*, Vol. 38, No. 11, 2007, pp. 2270–2282. https://doi.org/10.1016/j.compositesa.2006.11.009.

[39]   Turon, A., Camanho, P. P., Costa, J., and Dávila, C. G. "A Damage Model for the Simulation of Delamination in Advanced Composites under Variable-Mode Loading." *Mechanics of Materials*, 2006. https://doi.org/10.1016/j.mechmat.2005.10.003.

[40]   Turon, A., González, E. V., Sarrado, C., Guillamet, G., and Maimí, P. "Accurate Simulation of Delamination under Mixed-Mode Loading Using a Cohesive Model with a Mode-Dependent Penalty Stiffness." *Composite Structures*, Vol. 184, 2018, pp. 506–511. https://doi.org/10.1016/j.compstruct.2017.10.017.

[41]   Seneviratne, W., and Tomblin, J. Life of Composites under Variable-Amplitude Fatigue Using St Method. 2021.

[42]   Iarve, E. V., Hoos, K. H., Braginsky, M., Zhou, E., and Mollenhauer, D. H. "Progressive Failure Simulation in Laminated Composites under Fatigue Loading by Using Discrete Damage Modeling." *Journal of Composite Materials*, Vol. 51, No. 15, 2017, pp. 2143–2161. https://doi.org/10.1177/0021998316681831.

[43]   Francois, D. Fracture and Damage Mechanics of Concrete. In *Application of Fracture Mechanics to Cementitious Composites*, Springer Netherlands, Dordrecht, 1985, pp. 141–156.

[44]   Simo, J. C., and Ju, J. W. "Strain- and Stress-Based Continuum Damage Models—II. Computational Aspects." *International Journal of Solids and Structures*, Vol. 23, No. 7, 1987, pp. 841–869. https://doi.org/10.1016/0020-7683(87)90084-9.

[45]   Simo, J. C., and Ju, J. W. "Strain- and Stress-Based Continuum Damage Models—I. Formulation." *International Journal of Solids and Structures*, Vol. 23, No. 7, 1987, pp. 821–840. https://doi.org/10.1016/0020-7683(87)90083-7.

[46]   Seneviratne, W. p., and Tomblin, J. Life of Composites under Variable Amplitude Fatigue. 2021.

[47]   Pascoe, J. A., Alderliesten, R. C., and Benedictus, R. "Methods for the Prediction of Fatigue Delamination Growth in Composites and Adhesive Bonds – A Critical Review." *Engineering Fracture Mechanics*, Vols. 112–113, 2013, pp. 72–96. https://doi.org/10.1016/j.engfracmech.2013.10.003.

[48]   Khan, R., Alderliesten, R., Badshah, S., and Benedictus, R. "Effect of Stress Ratio or Mean Stress on Fatigue Delamination Growth in Composites: Critical Review." *Composite Structures*, Vol. 124, 2015, pp. 214–227. https://doi.org/10.1016/j.compstruct.2015.01.016.

[49]   Paris, P., and Erdogan, F. "A Critical Analysis of Crack Propagation Laws." *Journal of Basic Engineering*, Vol. 85, No. 4, 1963, pp. 528–533. https://doi.org/10.1115/1.3656900.

[50] Tao, C., Mukhopadhyay, S., Zhang, B., Kawashita, L. F., Qiu, J., and Hallett, S. R. "An Improved Delamination Fatigue Cohesive Interface Model for Complex Three-Dimensional Multi-Interface Cases." *Composites Part A: Applied Science and Manufacturing*, Vol. 107, 2018, pp. 633–646. https://doi.org/10.1016/j.compositesa.2018.02.008.

[51] Rosen, B. W. Mechanics of Composite Strengthening. 1965.

[52] Pinho, S., Davila, C. G., Camanho, P. P., Iannucci, L., and Robinson, P. *Failure Models and Criteria for FRP Under In-Plane or Three-Dimensional Stress States Including Shear Non-Linearity*. 2005.

[53] Argon, A. S. "Fracture of Composites." *Treatise on Materials Science and Technology*, 1972, pp. 79–114.

[54] Maimí, P., Camanho, P. P., Mayugo, J. A., and Dávila, C. G. "A Continuum Damage Model for Composite Laminates: Part II – Computational Implementation and Validation." *Mechanics of Materials*, Vol. 39, No. 10, 2007, pp. 909–919. https://doi.org/10.1016/j.mechmat.2007.03.006.

[55] Hoos, K., Iarve, E. V, Braginsky, M., Zhou, E., and Mollenhauer, D. H. "Static Strength Prediction in Laminated Composites by Using Discrete Damage Modeling." *Journal of Composite Materials*, Vol. 51, No. 10, 2017, pp. 1473–1492. https://doi.org/10.1177/0021998316651986.

[56] Raimondo, A., and Bisagni, C. "Fatigue Analysis of a Post-Buckled Composite Single-Stringer Specimen Taking into Account the Local Stress Ratio." *Composites Part B:*

Engineering, Vol. 193, 2020, p. 108000.

https://doi.org/10.1016/j.compositesb.2020.108000.

[57] Khan, R., Alderliesten, R., Badshah, S., and Benedictus, R. "Effect of Stress Ratio or

Mean Stress on Fatigue Delamination Growth in Composites: Critical Review."

Composite Structures, Vol. 124, 2015, pp. 214–227.

https://doi.org/10.1016/j.compstruct.2015.01.016.

[58] Joosten, M. W., Dávila, C. G., and Yang, Q. "Predicting Fatigue Damage in Composites

Subjected to General Loading Conditions." *Composites Part A: Applied Science and

Manufacturing*, Vol. 156, 2022, p. 106862.

https://doi.org/10.1016/j.compositesa.2022.106862.

[59] Raimondo, A., and Bisagni, C. "Analysis of Local Stress Ratio for Delamination in

Composites Under Fatigue Loads." *AIAA Journal*, Vol. 58, No. 1, 2020, pp. 455–463.

https://doi.org/10.2514/1.J058465.

[60] Dávila, C. G. "From S-N to the Paris Law with a New Mixed-Mode Cohesive Fatigue

Model for Delamination in Composites." *Theoretical and Applied Fracture Mechanics*,

Vol. 106, 2020, p. 102499. https://doi.org/10.1016/j.tafmec.2020.102499.

[61] ASTM. *Standard Test Method for Mode I Interlaminar Fracture Toughness of

Unidirectional Fiber-Reinforced Polymer Matrix Composites*. 2017.

[62] Seneviratne, W., Tomblin, J., and Walimunige, R. *Advanced Material Characterization &

Structural Certification*. 2020.

[63]   Hoos, K. H., Adluru, H. K., Van der Vossen, B., Makeev, A. V., and Iarve, E. V. *ADVANCED MATERIAL CHARACTERIZATION AND STRUCTURAL CERTIFICATION (AMCSC)*. 2020.
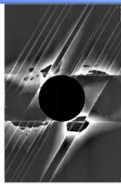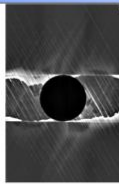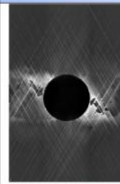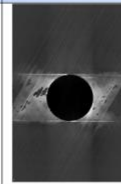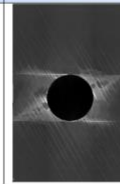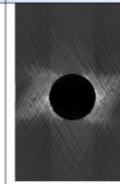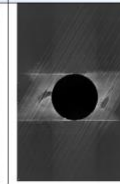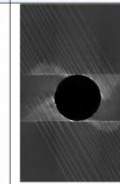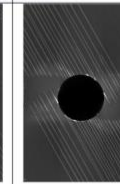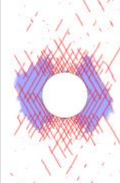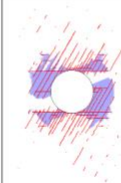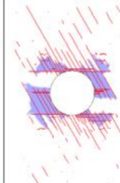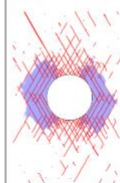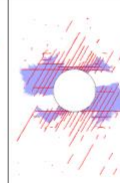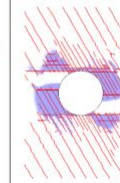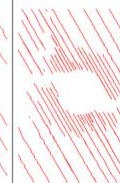
6 Appendix
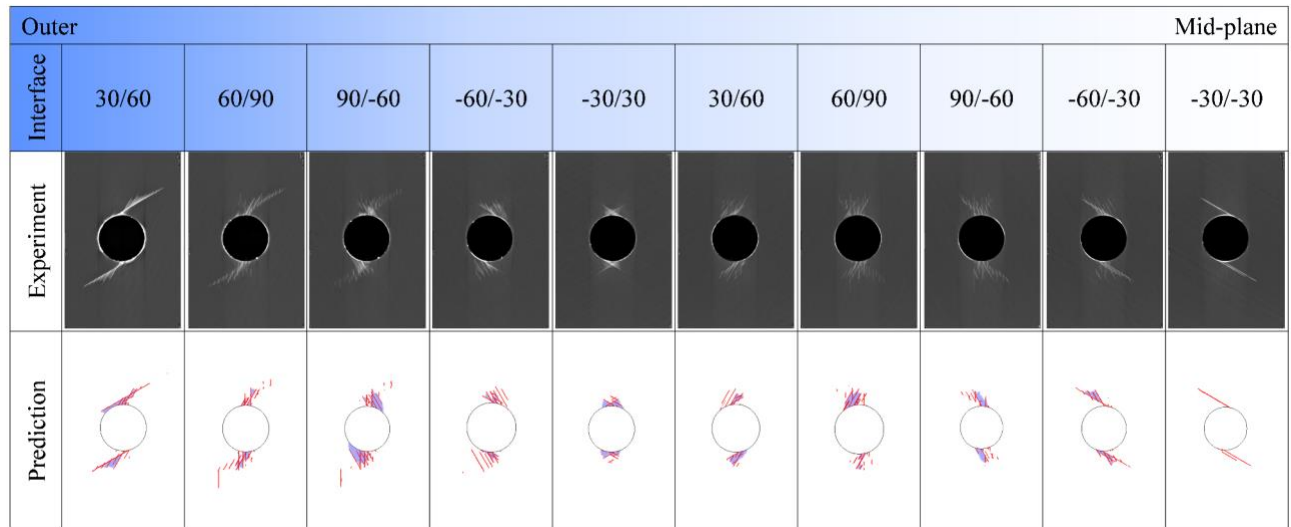

Figure 6.1 Matrix cracking and delamination comparison of the $[30°/60°/90°/−60°/−30°]_{2s}$ OHT specimen after 200k cycles for RXFEM/CZM Methodology Verificaiton
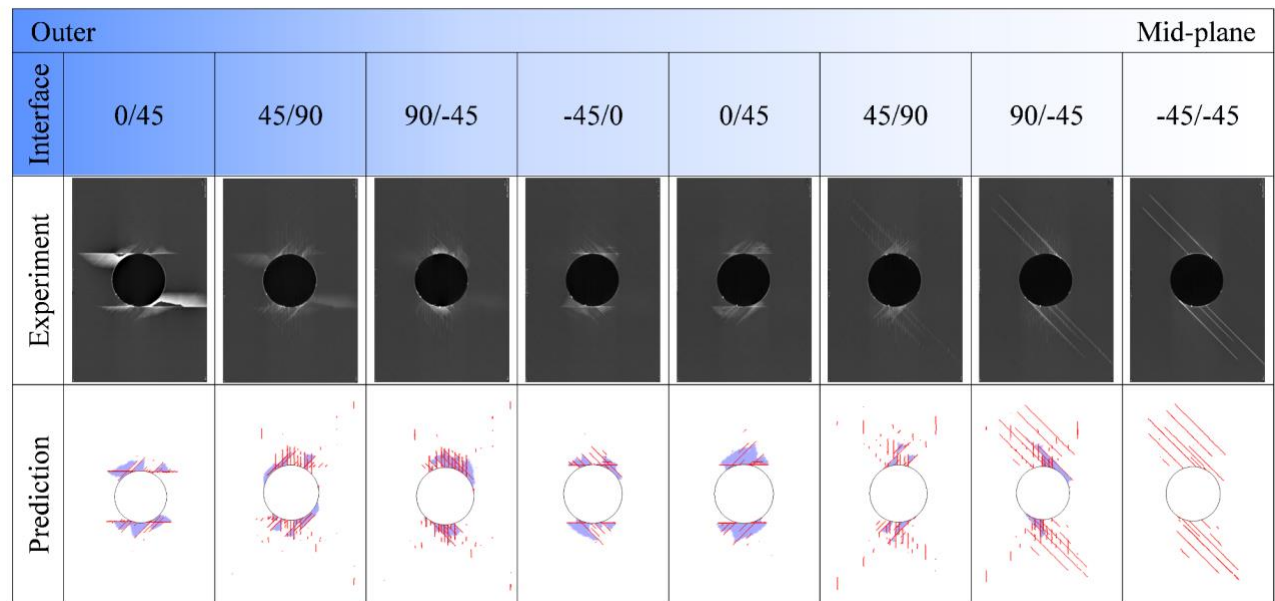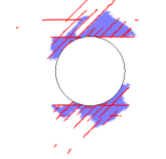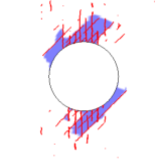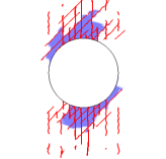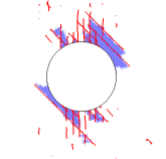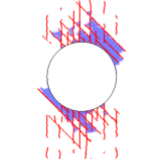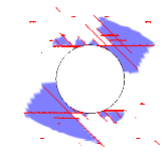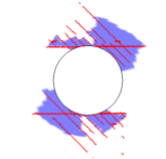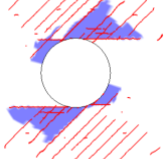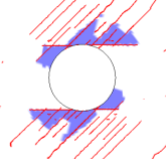

Figure 6.2 Matrix cracking and delamination comparison of the $[0°/45°/90°/−45°]_{2s}$ OHT specimen after 300k cycles for RXFEM/CZM Methodology Verificaiton

Figure 6.3 Matrix cracking and delamination comparison of the $[60°/0°/-60°]_{3s}$ OHT specimen after 200k cycles for RXFEM/CZM Methodology Verificaiton

Interface	IM7/5320-1	IM7/977-3
-45/90		
0/-45		
45/0		
90/45		
-45/90		
0/-45		
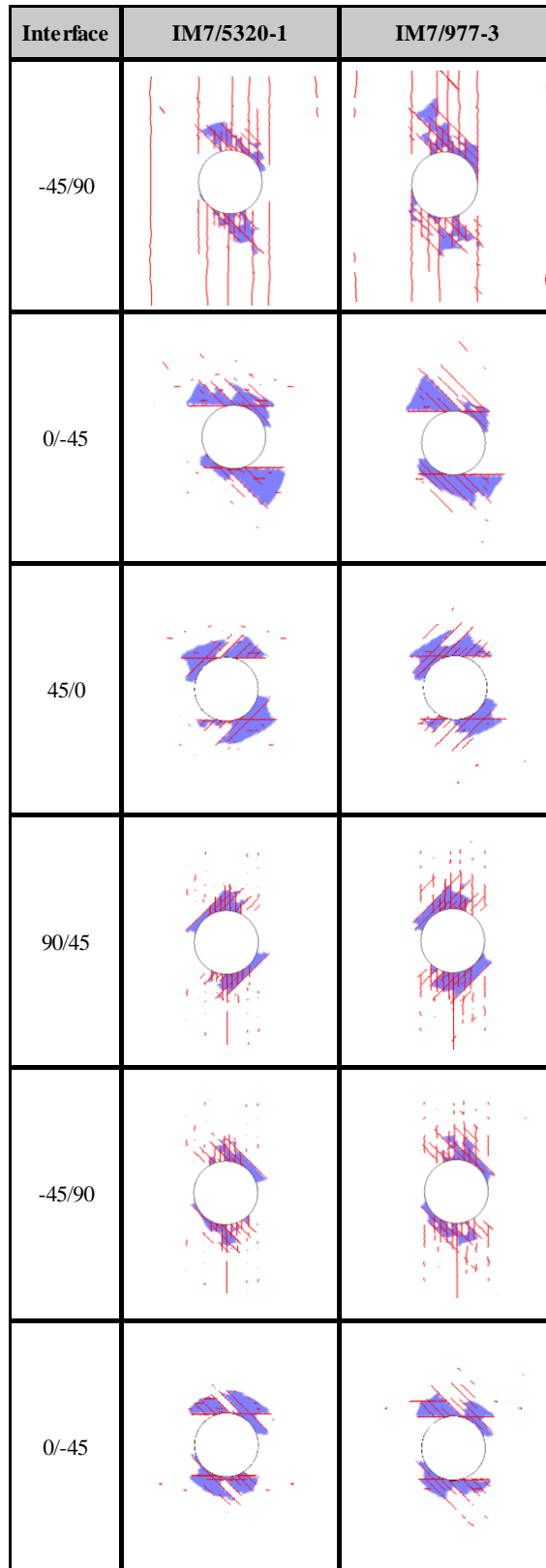
Figure 6.4 Inner ply fatigue damage of IM7/5320-1 and IM7/977-3 at 50k cycles

79

Interface	IM7/5320-1	IM7/977-3
45/0		
90/45		
-45/90		
0/-45		
45/0		

Figure 6.5 Outer ply fatigue damage of IM7/5320-1 and IM7/977-3 at 50k cycles